ADVANCING EARTH AND SPACE SCIENCES

JGR Solid Earth

RESEARCH ARTICLE
10.1029/2022JB026137

Paleomagnetic Constraint on the Age of the Shyok Suture Zone

Craig R. Martin[1,2], Oliver Jagoutz[1], Rajeev Upadhyay[3], Jill A. van Tongeren[4], Paul A. Mueller[5], and Benjamin P. Weiss[1]

[1]Department of Earth, Atmospheric, and Planetary Sciences, Massachusetts Institute of Technology, Cambridge, MA, USA, [2]Department of Earth and Planetary Sciences, University of Texas at Austin, Austin, TX, USA, [3]Department of Geology, Kumaun University, Nainital, India, [4]Department of Earth and Climate Sciences, Tufts University, Medford, MA, USA, [5]Department of Geological Sciences, University of Florida, Gainesville, FL, USA

Key Points:

- The Karakoram terrane was on the Eurasian margin at 20°N between 93 and 75 Ma
- The final closure of the Shyok suture zone occurred after 61.6 million years ago
- The Kohistan-Ladakh arc accreted onto India prior to final India-Eurasia continental collision

Supporting Information:

Supporting Information may be found in the online version of this article.

Correspondence to:

C. R. Martin,
crm7@mit.edu;
craig.martin@jsg.utexas.edu

Citation:

Martin, C. R., Jagoutz, O., Upadhyay, R., van Tongeren, J. A., Mueller, P. A., & Weiss, B. P. (2023). Paleomagnetic constraint on the age of the Shyok suture zone. *Journal of Geophysical Research: Solid Earth*, *128*, e2022JB026137. https://doi.org/10.1029/2022JB026137

Received 26 NOV 2022
Accepted 29 SEP 2023

Author Contributions:

Conceptualization: Craig R. Martin, Oliver Jagoutz
Formal analysis: Craig R. Martin, Paul A. Mueller
Investigation: Craig R. Martin, Oliver Jagoutz, Rajeev Upadhyay, Paul A. Mueller
Resources: Jill A. van Tongeren, Paul A. Mueller, Benjamin P. Weiss
Software: Paul A. Mueller
Supervision: Oliver Jagoutz, Benjamin P. Weiss
Writing – original draft: Craig R. Martin
Writing – review & editing: Craig R. Martin, Oliver Jagoutz, Rajeev Upadhyay, Paul A. Mueller, Benjamin P. Weiss

Abstract The India-Eurasia collision is a key case study for understanding the influence of plate tectonic processes on Earth's crust, atmosphere, hydrosphere, and biosphere. However, the timing of the final India-Eurasia continental collision is debated due to significant uncertainty in the age of the collision between the Kohistan-Ladakh arc (KLA) and Eurasia along the Shyok suture zone. Here we present paleomagnetic results that constrain the Karakoram terrane in northwest India to a paleolatitude of 19.9 ± 8.9°N between 93 and 75 million years ago (Ma). Our results show that the Karakoram terrane was situated on the southern margin of Eurasia in the Late-Cretaceous. Our results indicate that the KLA and Eurasian continent had a not converged until <61.6 Ma, placing a Paleocene older limit on the age of final closure of the Shyok suture zone. This suggests that the India-Eurasia collision in northwestern India likely occurred after the closure of the oceanic basin between the KLA and Eurasia. The Paleocene collision event affecting India that has been widely interpreted to represent final India-Eurasia collision instead records the arc-continent collision between the KLA and the northern edge of India prior to final India-Eurasia collision. Final India-Eurasia collision in northwest India most likely occurred after the closure of the oceanic basin between the KLA and Eurasia.

Plain Language Summary We use the magnetism of rocks to determine the latitude of the southern edge of Eurasia before the India-Eurasia continental collision. The results show that the southern edge of Eurasia was situated at 19.9 ± 8.9°N between 93 and 75 million years ago. This latitude means that a volcanic island chain called the Kohistan-Ladakh arc (KLA) was situated significantly south of the Eurasian continent at the start of the India-Eurasia collision. Our results suggest that the final stage of continental collision between India and Eurasia in northwest India occurred along the Shyok suture zone, a geological boundary where a major ocean basin once existed between the KLA and Eurasia.

1. Introduction

Collisions of continental plates are among the most significant tectonic events on Earth, affecting global plate configurations, climate and biological diversity. However, linking hydrosphere-biosphere processes and tectonic motion requires a detailed understanding of the tectonic events leading up to and during continental collisions. Robust reconstructions of pre-collisional configurations of the colliding plates are also essential for understanding the deformation mechanisms accommodating the shortening of continental plates during collision and orogenesis.

The classical case-study for investigating these processes is the Himalaya-Karakoram-Tibet orogenic belt in south Eurasia, which has conventionally been thought to be a single stage collision between India and Eurasia in the Paleocene related to the closure of the Neotethys Ocean (Gansser, 1964). However, in recent years, multiple studies have questioned this classical interpretation, and suggested a more protracted multi-stage collision (Aitchison & Davis, 2004; Aitchison et al., 2000; Bouilhol et al., 2013), similar to other ancient systems such as the Appalachian system. Multiple lines of evidence indicate that a major collision affected the northern Indian passive margin at 60–52 Ma, yet it is disputed whether this event dates the terminal India-Eurasia collision (DeCelles et al., 2014; Garzanti et al., 1987; Kaneko et al., 2003) or an earlier India-arc accretion (Aitchison et al., 2000; Jagoutz et al., 2015). An earlier collision could have involved an intra-oceanic arc system that developed in the ocean south of the Eurasian continental margin (Aitchison et al., 2000; Jagoutz et al., 2015; Martin et al., 2020) or a portion of the Gangdese magmatic arc and Xigaze forearc that rifted southward from Eurasia during mid-Late Cretaceous time (Kapp & DeCelles, 2019). Additionally, it has been proposed that the Indian plate rifted in the

Late Cretaceous and the Paleocene event relates to collision between Eurasia and a rifted India-derived fragment (van Hinsbergen et al., 2012; Yuan et al., 2021).

Multiple observations support and contradict each of these interpretations. The classic single-stage collision model requires that a vast amount of north-south India-Eurasia convergence (>3,000 km) was accommodated by continental shortening (Molnar & Stock, 2009). This is 1,000–2,000 km more than geologic observations suggest has been accommodated by deformation within Tibet (van Hinsbergen et al., 2011) and within the Himalaya fold and thrust belt (DeCelles et al., 2002). Additionally, major faults accommodating the collision, like the Red River shear zone, Altyn Tagh fault, and Gangdese/Kailash thrust were mostly active after 40 Ma (Cowgill et al., 2003; Leloup et al., 2001; Yin et al., 1999), and major collision-related melting, migmatization and leucogranite emplacement in the Himalayan belt is younger than 45 Ma (Aikman et al., 2008; Burg & Bouilhol, 2019).

The India-arc accretion model reinterprets the Paleocene collision as the accretion of a trans-Tethyan intra-oceanic subduction zone/arc system onto India prior to the final India-Eurasia collision at 40–45 Ma (Aitchison et al., 2000; Bouilhol et al., 2013; Jagoutz et al., 2015). In this model, the subduction of an oceanic plate between India and Eurasia after the Paleocene onset of arc-continent collision provides a plausible mechanism to accommodate the excess convergence not accounted for in geological estimates (Martin et al., 2020). Oceanic lithosphere would not be represented in shortening estimates because it was subducted into the mantle (Cloos, 1993). Geological evidence for this model derives from the western and eastern peripheries of the system (Ladakh, Pakistan, and Myanmar), but may not be supported by the geology of the central part of the system where there is limited evidence for an additional arc terrane south of the Gangdese arc (Wang et al., 2017).

Of particular importance in this discussion is constraining the relative locations and motions of the active southern margin of Eurasia, the trans-Tethyan intra-oceanic subduction zone, and the pre-collision extent of the Indian continental lithosphere. Unfortunately, the narrow suture zones that transect the Himalayan belt preserve only fragmentary records. In the central and eastern Himalaya, Indian passive margin sedimentary rocks are directly juxtaposed against elements of the southern-Eurasian active margin along major post-Miocene backthrusts that overprinted the complex Yarlung-Tsangpo suture zone (Burg & Chen, 1984; Yin et al., 1999). In the western Himalaya, Indian and Eurasian terranes are separated from one another by the Kohistan-Ladakh arc (KLA), a large remnant of an intra-oceanic subduction system that operated in the Neotethys prior to the continental collision (Tahirkheli, 1979). The southern boundary between the KLA and India is delineated by the Indus suture zone, and in the north, the Shyok suture zone separates the KLA from the Karakoram terrane, part of southern Eurasia since the Jurassic (Tahirkheli, 1979; Zanchi et al., 2000). The Karakoram terrane comprises a pre-Ordovician metamorphic basement complex overlain by Ordovician–Cretaceous sedimentary rocks and intruded by the Cretaceous Karakoram Batholith (Zanchi et al., 2000).

Crucially, a prediction of the Paleocene arc-continent accretion model is that the age of collision along the Indus suture zone reflects arc accretion onto India prior to final collision and that final closure of the Shyok suture occurred afterwards, that is, younger than 55–50 Ma (Garzanti et al., 1987; Kaneko et al., 2003; Najman et al., 2017). Unfortunately, the closure age of the Shyok suture zone has remained an open question: previous estimates range from >80 Ma (Borneman et al., 2015; Petterson & Windley, 1985) to as young as 40 Ma (Bouilhol et al., 2013; Brookfield & Reynolds, 1981), spanning times before and after the closure of the Indus suture zone.

Previous Cretaceous age constraints for the Shyok suture zone have been based on detrital zircon provenance investigations seeking to distinguish Karakoram-, KLA-, and India-derived detrital zircon populations to constrain the timing of sediment co-deposition from converging terranes as a proxy for collision (Borneman et al., 2015; Najman et al., 2017). Detrital zircon provenance studies of sedimentary rocks deposited on the Indian plate have provided strong evidence for a collision between the Indian plate and a volcanic arc and some Eurasian-derived source rocks at 60–55 Ma (DeCelles et al., 2014; Garzanti et al., 1987; B. Hu et al., 2012; X. M. Hu et al., 2015; Najman et al., 2017; Wu et al., 2010). However, these observations do not necessarily constrain final closure of the Shyok suture zone nor final India-Eurasia collision because the KLA provides a plausible source for Cretaceous arc-related detritus on the northern Indian passive margin. The KLA also provides a plausible source of other Eurasia-derived detrital zircons because it may have

formed close to the Eurasian margin and subsequently rifted southward, could have joined with the Eurasian margin along strike, or could have been built on Eurasian crustal fragments (Kapp & DeCelles, 2019; Rolland et al., 2000; Saktura, Buckman, Aitchison, & Zhou, 2021). These challenges are compounded by the potential for zircon transport over thousands of kilometers during along-trench sediment transport (Thornburg & Kulm, 1987).

Changes in the εHf and εNd isotopic composition of KLA arc-magmas at 40.4 ± 1.3 Ma have also been used as a constraint on KLA-Eurasia collision (Bouilhol et al., 2013), however, this approach relies on complex magmatic processes taking place at depth and so is an indirect constraint. Another indirect constraint includes the >84 Ma age of an unconformity in which folded sedimentary rocks sit atop metamorphosed Jurassic strata in Pakistan that was interpreted as bracketing metamorphism related to the KLA-Eurasia collision (Gaetani et al., 1990, 1993). However, this unconformity does not overlie the Shyok suture zone, nor the Kohistan arc (Gaetani et al., 1990), so it does not directly constrain the age of the KLA-Eurasian collision. The fining upwards sequence of marine sedimentary strata above the unconformity (Gaetani et al., 1990) suggests a subsiding marine basin north of the KLA at this time rather than a post-collisional terrestrial environment.

To provide additional constraints on the age of the Shyok suture zone, here we compare two paleomagnetic poles obtained from rocks just 15 km apart on either side of the Shyok suture zone in Ladakh, northwest India. Our new paleomagnetic results are derived from Late Cretaceous volcanic and sedimentary rocks deposited in a forearc setting on the Karakoram margin. They enable us to directly compare the paleolatitude of the Karakoram terrane with that of the KLA previously obtained from the Khardung volcanics by Martin et al. (2020). If the KLA had accreted onto the Eurasian margin long prior to the India-Eurasia collision and remained there since ∼80 Ma, then the Karakoram terrane and KLA should share a similar paleolatitude. Alternatively, a significant difference in paleolatitude would imply a separation between the KLA and Karakoram blocks that would preclude final closure of the Shyok suture zone until after the 66.1–61.6 Ma formation of the Khardung volcanics. Our results show a significant difference between the paleopoles and confirm that an ocean basin existed between the Karakoram and KLA as collision was beginning on the northern edge of India in the Paleocene. While the pre-Paleocene paleogeography of the KLA and extent of intra-oceanic subduction in the Neotethys ocean during the Cretaceous remains uncertain, our results show that the Paleocene collision event in the western Himalaya was the accretion of the KLA onto India prior to final continental collision.

2. Geological Background

The Shyok suture zone (see Figure 1) is a complex zone that records not only the collision between the KLA and Eurasia, but also significant strike-slip faulting and thrusting associated with the indentation of India into Eurasia (Coward et al., 1986). We studied the Shyok suture zone at its easternmost exposure where it is well exposed and accessible in the border area of northern Ladakh in northwestern India. There, the Shyok suture is dominated by a 152–159 Ma forearc ophiolite comprising pyroxenites, serpentinites, gabbros, diorites, and pillow basalts (Changmar/Bogdang Ophiolite) that are overlain by a thick sequence of subduction-related basalt and basaltic andesite volcanics (Shyok volcanics) (Rolland et al., 2000; Saktura, Buckman, Nutman, & Bennett, 2021; Srimal, 1986; Thanh et al., 2012). The ophiolite and volcanics are unconformably overlain by the middle to late-Cretaceous Hundri Formation, which is composed of shallow-marine limestone, shale, and chert (Srimal, 1986; Upadhyay, 2014).

To the south, the ophiolitic and forearc units are in faulted contact (Srimal, 1986) with either the Khardung volcanics or the Ladakh Batholith, which comprise the extrusive and intrusive elements, respectively, of the KLA (Dunlap & Wysoczanski, 2002). The Khardung volcanics are composed of rhyolite, dacite, tuff and volcano-sedimentary flows that are now in faulted contact with, but thought to be originally deposited over and subsequently intruded by, successive plutonic phases of the Ladakh batholith (Bhutani et al., 2009; Dunlap & Wysoczanski, 2002). The volcanics have an age range of 66.1–61.6 Ma (Lakhan et al., 2020; Martin et al., 2020), and may extend to as young as 51.9 Ma at their uppermost exposure (Saktura, Buckman, Aitchison, & Zhou, 2021). A north-dipping thrust-reactivated normal fault (Saltoro fault) separates the marine forearc sedimentary sequence of the Hundri Formation from the fluvial and estuarine sedimentary strata and volcanics of the Saltoro Formation (Srimal, 1986; Upadhyay et al., 1999). This structure underlies an angular unconformity that was initially misinterpreted as the basal contact of the Saltoro Formation by Borneman et al. (2015). The unconformity is situated

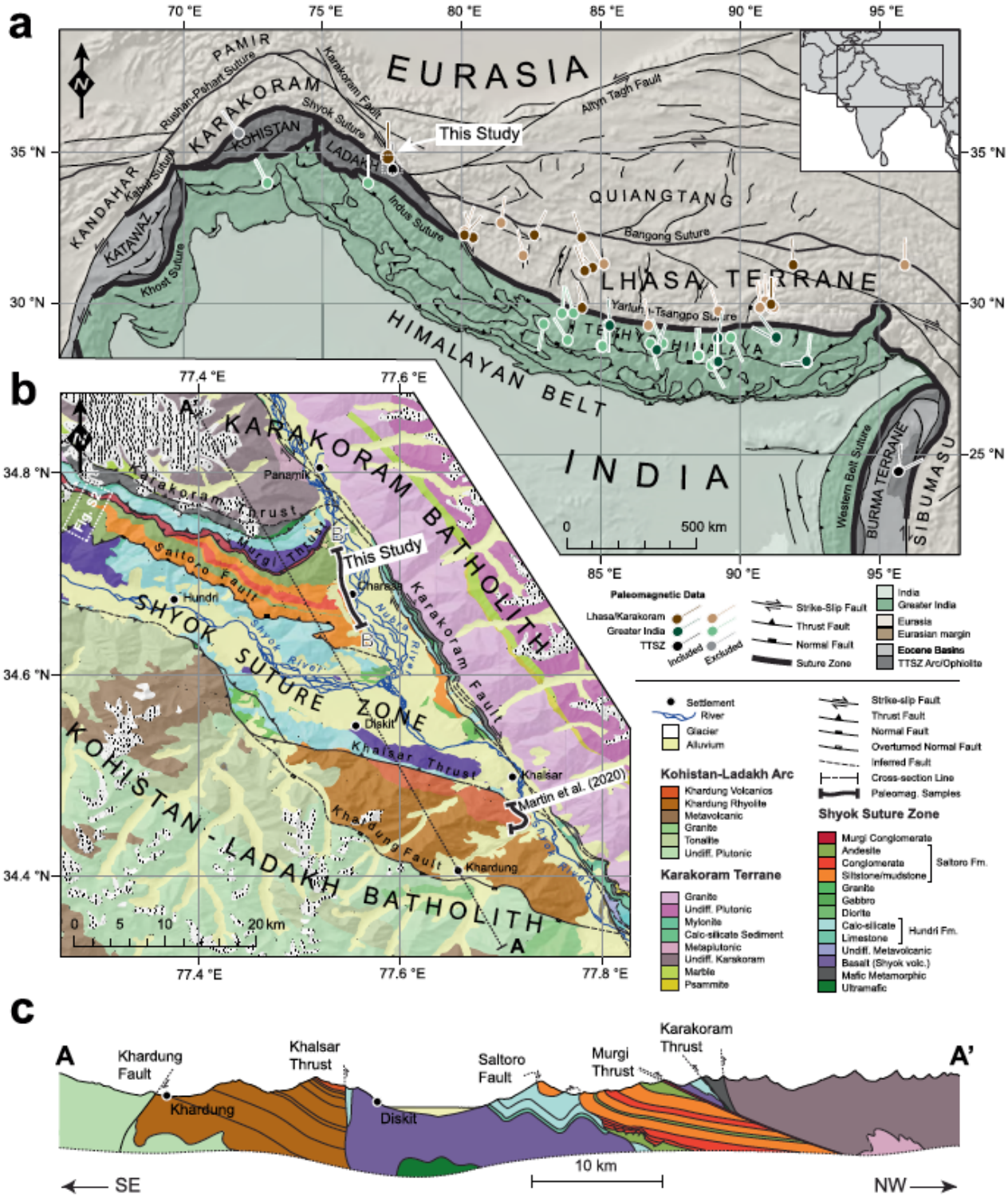

Figure 1. Geologic maps of the Himalaya and Nubra-Shyok confluence area in Ladakh NW India. (a) Tectonic map showing the architecture of the Himalayan orogenic belt from Afghanistan to Myanmar with Indian derived terranes (green), Eurasian tectonic blocks (brown), and intra-oceanic arc remnants (dark gray) shown in contact with each other along major faults (narrow black lines) and suture zones (thick black lines). Paleomagnetic study locations and the mean paleomagnetic declinations are overlaid on the terranes where they were derived, with darker shading indicating the most reliable paleomagnetic studies (see Table S6 in Supporting Information S2). (b) Detailed geological map of the Shyok suture zone in the Shyok-Nubra confluence area, Ladakh, northwest India. The major structures and tectonostratigraphic units of the Shyok suture zone are overlaid with the locations of the paleomagnetic sampling sections for the Saltoro Formation (this study) and the Khardung volcanics (Martin et al., 2020). (c) Geological cross-section at 1:1 scale for the line marked A–A' that is oriented southeast to northwest (330°) from the Kohistan-Ladakh Batholith near the village of Khardung across the Shyok suture zone to the Karakoram terrane.

within the lower Saltoro Formation and is associated with syn-sedimentary extensional faulting (see Figure S1 in Supporting Information S1). The Saltoro Formation comprises a wedge that is tilted toward the northwest and is truncated at its upper contact by a complex set of late-stage south-vergent thrusts representing the eastern extent of the Karakoram thrust system (Rai, 1982; Rex et al., 1988; Rolland et al., 2000; Searle et al., 1989). The tilt of the Saltoro Formation strata steepens to vertical toward the south where the strata are folded into a north-verging anticline.

We studied an approximately 5,342 m thick exposure of the Saltoro Formation on the western bank of the Nubra valley near the village of Charasa (see Figure 1). The base of the Saltoro stratigraphy is not exposed in the study area, but the lowermost 220 m of the exposed sedimentary sequence comprises primarily fine-grained fluvial sandstones interbedded with poorly sorted conglomerates containing a variety of well-rounded pebble and cobble size clasts of almost entirely extrusive volcanic lithologies, as well as rare granite, sandstone, shale, limestone and chert clasts (see Figure S2a in Supporting Information S1). Over the next 560 m of the stratigraphy, the conglomerates grade upwards into 0.3–2 m thick layers of sandstone sometimes with planar crossbedding interbedded with 1–5 cm thick siltstone and mudstone horizons with symmetrical ripples (see Figure S2b in Supporting Information S1). The dominant grain-size continues to decrease for a further 720 m up section, becoming characterized by mudstones and siltstones interbedded with fine-grained sandstones. Periodically, coarse-grained sandstone beds interbedded with the finer-grained layers indicate periods of high sediment transport and stronger flow conditions.

At a stratigraphic level of 1,510 m above the lowermost exposed strata, in the distinctive promontory upon which the Charasa Monastery is situated, there is a 50–120 m thick, internally homogeneous and laterally continuous plagioclase-pyroxene porphyritic andesite flow. Phenocrysts vary in size from 0.5–2 cm and are sometimes clustered together into glomerocrysts. The upper surface of this volcanic unit contains weathering cracks that are filled with the overlying coarse sandstone (see Figure S2c in Supporting Information S1). The Charasa Monastery volcanic flow is overlain by a 715 m thick section of sedimentary strata comprising fine-grained gray and red mudstones interbedded with medium- to coarse-grained sandstones. This section is overlain by a 40 m thick conglomerate unit that marks the start of a break in section due to Quaternary cover. Above the break, 480 m of mudstones and shales give way to massive volcaniclastic tuffs and agglomerates. The agglomerates have 2–15 cm diameter subangular clasts in a fine-grained welded matrix and are increasingly interbedded with very fine-grained black basalts and basaltic andesites up section toward the north.

Volcanic flows dominate the 2,290 m thick uppermost section of exposed Saltoro stratigraphy. The andesitic and trachyandesitic volcanics are very fine-grained, unfoliated, and sometimes contain 1–5 mm long plagioclase phenocrysts and/or vesicles. Some of the volcanic flows are locally epidotized and exhibit spectacular auto-brecciation (see Figure S2d in Supporting Information S1), suggesting that some flows were erupted into lacustrine or shallow marine environments. In places the basalts are interbedded with black medium- to coarse-grained lithic sandstones. The presence of major volcanic flows conformably bedded with the sedimentary horizons throughout the Saltoro stratigraphy indicates that the sedimentary rocks accumulated in close proximity to active volcanic centers. The Saltoro Formation is crosscut by small 0.5–3 m wide intermediate and felsic dikes.

3. Materials and Methods

3.1. Geochronology

To extract zircons for U-Pb geochronology that could constrain the age range of our paleomagnetic results, we collected oriented block samples from throughout our paleomagnetic sample section. The rock samples were disaggregated by manual sledging, pulverized using a Shatterbox and sieved into monomineralic, sand sized particles. Magnetic and density separation techniques were used to obtain dense mineral concentrates from which zircon grains were randomly sampled and mounted in epoxy resin with natural reference standards and polished to expose the interiors of the grains. Zircons were imaged using backscattered electron (BSE) and cathodoluminescence using a scanning electron microscope (SEM) at MIT. Using the imagery to guide spot targeting, samples were dated with laser ablation inductively coupled plasma mass spectrometry (LA-ICP-MS) at the University of Florida and Rutgers University. Details of measurement protocols are in Mueller et al. (2008).

Data reduction was completed at Rutgers University using the Iolite software package (Paton et al., 2011) and at University of Florida using in-house software (Calamari). In order to minimize the chance of age underestimation due to lead loss (Vermeesch, 2021) we filtered our data using a 5% discordance cutoff and only included analyses with $^{204}Pb/^{206}Pb < 0.001$. The discordance filter used the discordance between the $^{206}Pb/^{238}U$ age and $^{207}Pb/^{235}U$ age for zircons with $^{206}Pb/^{238}U$ ages less than 1,000 Ma and the discordance between the $^{206}Pb/^{238}U$ age and $^{206}Pb/^{207}Pb$ age for zircons with $^{206}Pb/^{238}U$ age greater than 1,000 Ma. All geochronology data shown in supplementary Table S1 in Supporting Information S2. Concordia diagrams and detrital zircon spectra (see Figure S3 in Supporting Information S1) were produced using the AgeCalcML software package (Sundell et al., 2021).

3.2. Paleomagnetism

We collected 7–10 oriented core samples from 34 horizons distributed throughout the Saltoro Formation stratigraphy near Charasa for paleomagnetic analysis. Bedding orientations at each site were measured repeatedly over a 20–40 m along-strike and the bedding orientation used for structural corrections are the mean of 5–15 individual measurements. Andesite bedding horizons were identified using chilled upper surfaces of beds. Core samples were collected in the field using a water-cooled electric hand drill and oriented using an ASC Industries Pomeroy orienting fixture. Nonmagnetic brass tools were used to extract cores from the outcrop to prevent damaging the remanent magnetization of samples during sample collection. Optical microscopy was used to identify magnetic carriers and textural relationships within the samples. One specimen was cut from each core sample using an ASC Scientific dual-blade rock saw. The natural remanent magnetization was measured on a 2G Enterprises Superconducting Rock Magnetometer equipped with an automated sample handler (Kirschvink et al., 2008) inside a mu-metal magnetically shielded room in the MIT Paleomagnetism Laboratory applying a <200-nT DC field. Specimens were subjected to stepwise alternating field (AF) and thermal demagnetization and complete demagnetization data is available at Dryad (Martin et al., 2023). AF steps were applied in increments of 2 up to 12 mT followed by thermal steps starting at 100°C and increasing up to 600°C or 680°C in variable interval sizes from a maximum of 100°C and minimum of 2°C close to the Curie temperatures of the suspected principal magnetic carriers (magnetite: 580°C, and hematite: 680°C). Stable components of magnetization were isolated using principal component analysis (Kirschvink, 1980) (see Table S2 in Supporting Information S2). Origin trending components were anchored to the origin and components were only fitted where the maximum angular deviation was <15°.

The magnetic carrier phases in representative samples were characterized with BSE imaging using a SEM at MIT, as well as thermomagnetic susceptibility measurements using a KLY-2 Kappabridge magnetic susceptibility system at the Institute for Rock Mmagnetism at the University of Minnesota. Hysteresis curves were acquired for applied fields of −1 to 1 T and corrected by removing any paramagnetic or diamagnetic signals. Samples were analyzed using an ADE model 1,660 vibrating sample magnetometer in the Ross Laboratory, MIT Department of Materials Sciences and Engineering.

Site-mean magnetization directions were calculated using Fisher statistics (Fisher, 1953), and corrected for bedding tilt. Corrections for inclination-shallowing of sedimentary magnetization directions were made using the elongation-inclination method of Tauxe and Kent (2004). Northern hemisphere virtual geomagnetic pole (VGP) positions for each site were determined and the Fisher mean (Fisher, 1953) of the VGP data was used to obtain the overall paleomagnetic mean pole and associated A_{95} error envelope (see Table S3 in Supporting Information S2). All paleomagnetic data processing and plotting were done using the PmagPy software package (Tauxe et al., 2016).

4. Results

4.1. U/Pb Geochronology

Detrital zircons from four sedimentary samples, comprising three medium-fine grained sandstones (LB19-06, LB18-18, and LB18-20) and one siltstone (LB19-54), were analyzed along with one sample of welded tuff (LB19-56) to bracket the age of deposition/eruption of the paleomagnetic sampling section (see Figure 2). In the subsequent section, we report the $^{206}Pb/^{238}U$ age and 2σ uncertainty of the youngest individual zircon in each sample (Coutts et al., 2019; Dickinson & Gehrels, 2009). In cases where the youngest grain had a large 2σ

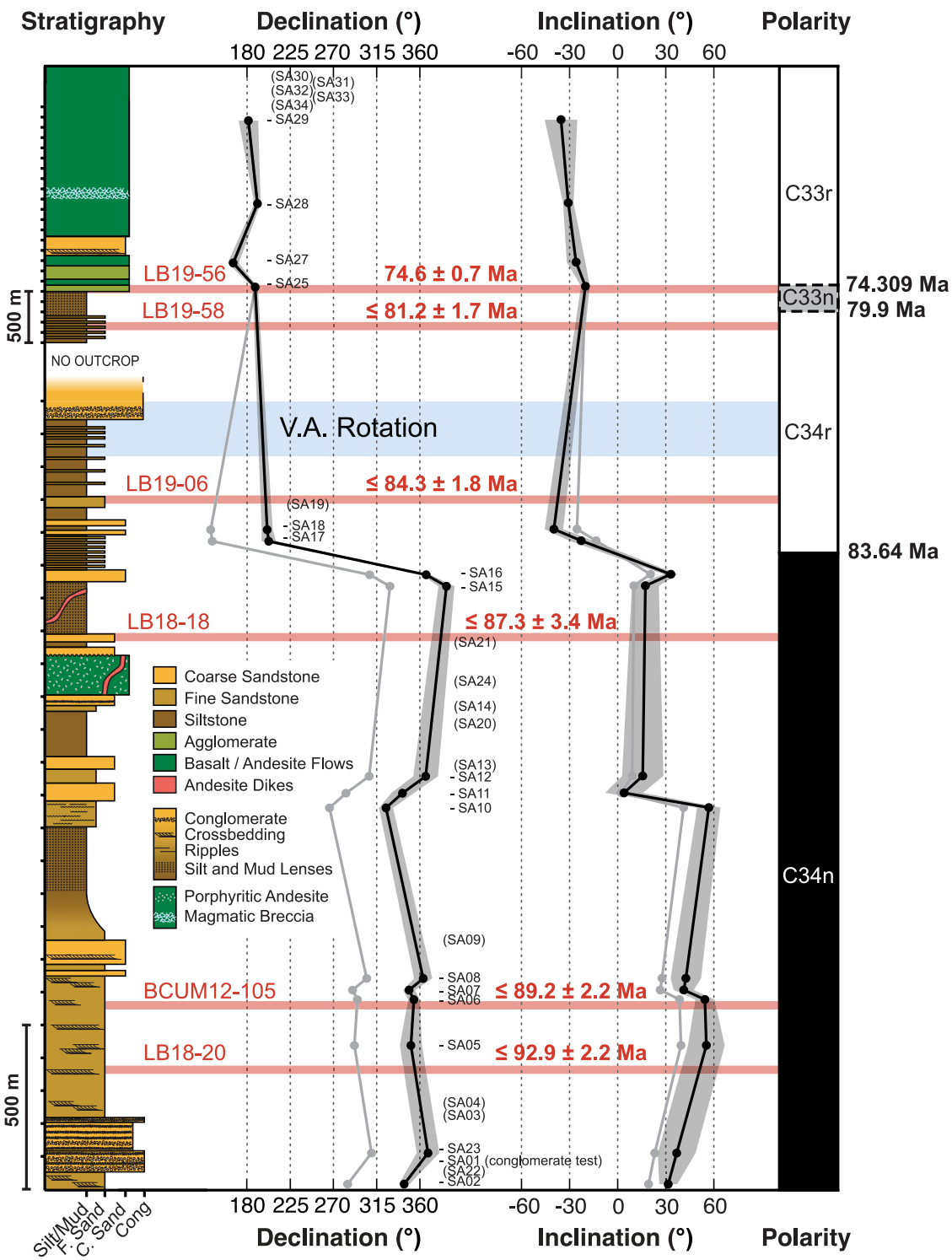

Figure 2. Stratigraphic column of the Saltoro Formation showing the change in lithology with increasing stratigraphic height. Red bars indicate U-Pb zircon ages from this study and the recalculated age from sample BCUM12-105 of Borneman et al. (2015). The blue bar indicates the approximate stratigraphic height at which a counterclockwise vertical axis rotation (VAR) is present in the paleomagnetic data set. The black lines and points show the inclination and declination of the paleomagnetic sites with the 95% uncertainty displayed using shading around the line. The gray lines and points show the declination and inclination of the paleomagnetic data prior to corrections for the VAR and inclination shallowing due to compaction. The ages were used to correlate the magnetic declination and inclination of our paleomagnetic sites with the known geodynamo reversal C34n to C34r (Gradstein et al., 2020), shown using the chronostratigraphic bar on the right.

uncertainty we report the $^{206}Pb/^{238}U$ age of the zircon with the smallest 2σ uncertainty that was within error of the youngest zircon in the same sample. The age of the tuff sample records the time of magma cooling and eruption while the detrital zircon ages are maximum depositional ages because the true depositional age is by definition an unknown amount younger than the youngest zircons in the sample. Nevertheless, the presence of volcanic flow horizons within the Saltoro stratigraphy indicates that active volcanic centers were proximal to the sedimentary catchment area, so the maximum depositional ages we obtained are likely very close to the actual depositional age of the sample.

At the base of our sampled section, sample LB18-20 yielded a maximum depositional age ≤92.9 ± 2.2 Ma. This age is identical within error to the ≤92.43 ± 0.24 Ma age that Borneman et al. (2015) obtained from their sample BCUM12-105, collected up-section of LB18-20. The weighted mean of the youngest peak method employed by Borneman et al. (2015) likely overestimates the true depositional age compared to the youngest single grain method employed in this study (Coutts et al., 2019; Vermeesch, 2021). For comparison with our data, we passed the data from Borneman et al. (2015) sample BCUM12-105 through the same quality filter applied to our data and derived a youngest single grain maximum depositional age estimate ≤89.2 ± 2.2 Ma. Both the originally reported age and our recalculated age produce younger ages up-section, but our treatment of their data appears to provide a closer approximation of the true maximum depositional age of the sample along with more realistic uncertainty.

Sample LB18-18 is from a fine-grained sandstone deposited directly above the andesitic flow exposed at the Charasa Monastery. It yielded a maximum depositional age ≤85.3 ± 3.4 Ma. Sample LB19-06 is from a medium-grained sandstone interbedded with mudstones in the middle portion of the sampled Saltoro section. It yielded a maximum depositional age ≤84.3 ± 1.8 Ma. A small break in exposure due to Quaternary glacial cover separates LB19-06 from the overlying sedimentary strata, volcaniclastics, and thick volcanic flow succession that defines the uppermost exposures of the Saltoro Formation stratigraphy. LB19-58 is a fine-grained siltstone near the base of this upper exposure and yielded a maximum depositional age ≤81.2 ± 1.7 Ma. The youngest age constraint on the sampled section comes from the welded tuff sample (LB19-56) that yielded a well-defined population of igneous grains along with a few xenocrysts. The U-Pb zircon age of the tuff is 74.6 ± 0.7 Ma. This provides a younger bound on most of our paleomagnetic samples, with four accepted paleomagnetic sites situated higher in the stratigraphy where no viable sample for U-Pb geochronology was available.

The U-Pb zircon depositional and eruption ages of our samples are consistently younging up-section (see Figure 2), suggesting that there are no major structural breaks (e.g., overthrusts) or unconformities throughout the section. The results also suggest that the time interval recorded in our paleomagnetic sampling section is 18.3 million years in the Late Cretaceous between 92.9 ± 2.2 and 74.6 ± 0.7 Ma. This interval spans sufficient time for the paleomagnetic data to reliably average paleosecular variation (PSV) of the geodynamo (Deenen et al., 2011).

All the sedimentary samples (LB18-20, LB18-18, LB19-06, LB19-54) contained detrital zircons with broad, multi-peaked age distributions ranging from the late Cretaceous to the Mesoarchean with most of the grains yielding Cretaceous or Jurassic ages (see Figure 3). The detrital zircon age spectra are consistent with those of similar age sedimentary strata from Eurasian margin sources, including the Lhasa terrane, Central Pamir, Qiangtang terrane, and the Xigaze Forearc basin (Chapman et al., 2018a; DeCelles et al., 2007; Gehrels et al., 2011; He et al., 2019; Robinson et al., 2012; Xue et al., 2022). This suggests that the Shyok suture zone sedimentary sequence and underlying Jurassic ophiolite were proximal to the Eurasian active margin from 92.9–74.6 Ma (Borneman et al., 2015).

4.2. Characterization of Remanence Carriers

Samples of a siltstone from site SA06, a sandstone from site SA17, and an andesite from site SA25 were imaged using a SEM. The sedimentary samples contained abundant detrital magnetite/titanomagnetite grains with diameters of 5–150 μm that were often associated with titanohematite/hematite alteration textures (see Figure S4 in Supporting Information S1). The andesite sample from site SA25 contained well preserved euhedral magnetite/titanomagnetite crystals with 2–30 μm size. These grains were sometimes associated with minor titanohematite/hematite overgrowths (see Figure S4 in Supporting Information S1). The titanohematite/hematite in our samples is likely a secondary paragenesis (overprint) acquired some unknown time after deposition while the magnetite/titanomagnetite appears primary.

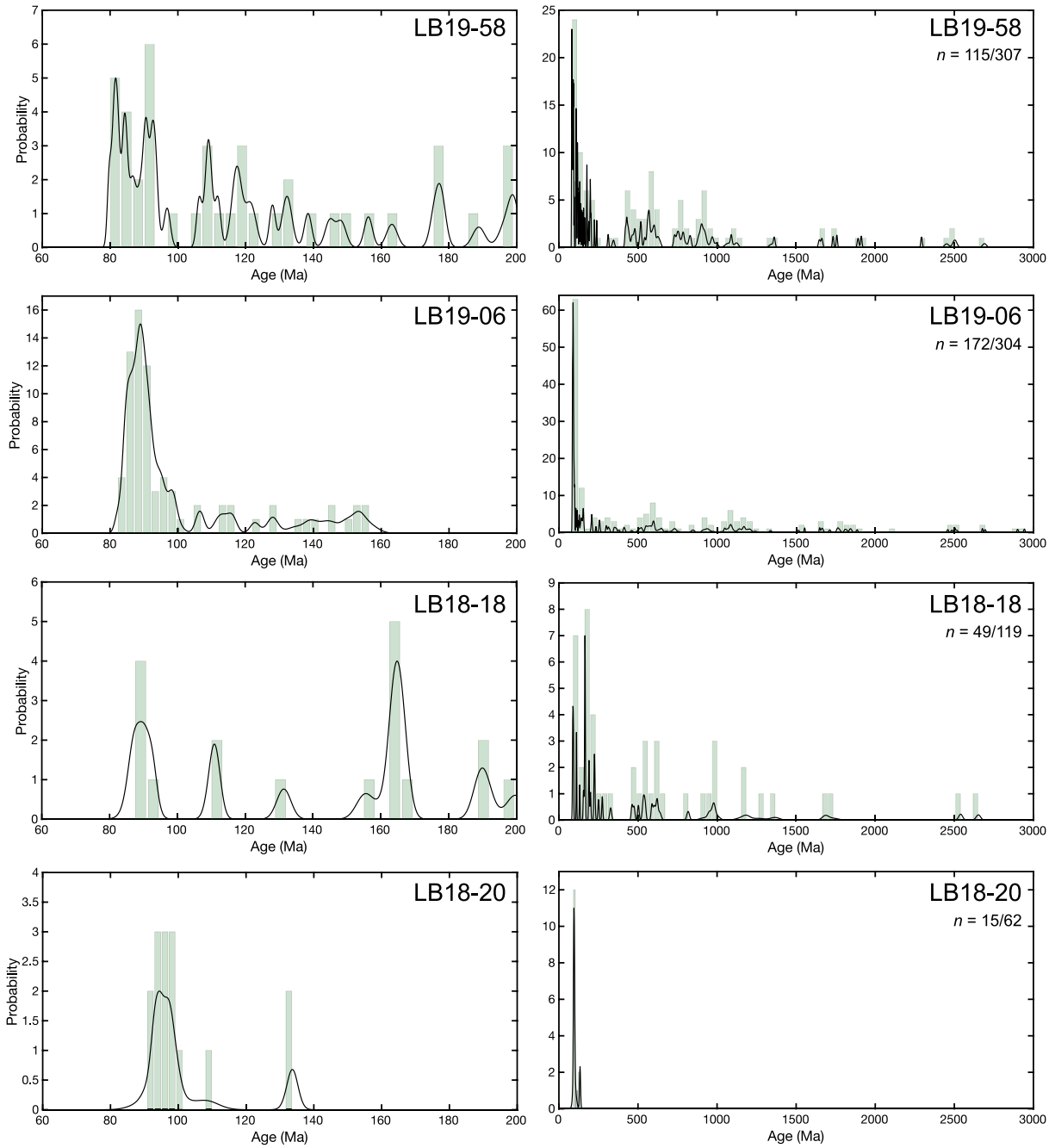

Figure 3. Histograms and probability density distributions of detrital zircon U-Pb ages that passed the <5% discordance criterion. The right panels show the full detrital age spectrum including all the grains present in the sample, the left panel shows just the grains with U-Pb ages <200 Ma.

We also obtained susceptibility versus temperature curves for a suite of four volcanic samples (SA24-7, SA25-3, SA27-5, and SA28-7) and four sedimentary samples (SA03-1, SA07-6, SA16-1, and SA23-5) that are representative of the range of lithologies studied (see Figure S5 in Supporting Information S1 and Table S4 in Supporting Information S2). Low temperature analyses yielded no major transitions except for samples SA24-7 and SA16-1, which exhibited a small susceptibility drop between 280 and 350°C indicative of either minor pyrrhotite or high-Ti magnetite (Dunlop & Özdemir, 1997). High temperature analyses of volcanic samples exhibited unblocking temperatures of 565–580°C and a Hopkinson peak near the curie temperature typical of the presence of single domain (SD) and pseudo-single domain (PSD) magnetite (Dunlop & Özdemir, 1997). Sedimentary samples SA03-1, SA23-5 and SA16-1 had unblocking temperatures between 550 and 580°C and Hopkinson peaks near

the Curie temperature, indicating the presence of SD and PSD magnetite. The data from SA07-6 was too noisy to interpret. The curves for all the samples were irreversible during cooling below 700°C, indicating that some magnetic phases (likely magnetite) were created during heating.

Hysteresis curves were acquired for a representative subset of volcanic samples (SA24-7, SA27-5, and SA28-7) and for representative sedimentary samples (SA16-1, SA17-2, SA19-3, and SA22-5) exhibiting different component combinations as determined by their thermal demagnetization results (see Figure S6 in Supporting Information S1). The hysteresis curves were corrected for paramagnetic and diamagnetic signals and used to determine the saturation magnetization (M_s), the saturation remanent magnetization (M_{rs}), the coercivity of remanence (H_{cr}), and the coercivity (H_c) for each sample (see Table S5 in Supporting Information S2).

4.3. Paleomagnetism

The sample set contains a broad spectrum of lithologies exhibiting a range of different magnetic components characterized by different unblocking temperatures and relative magnitude (see Figure 4). Almost all specimens exhibited a low temperature and low coercivity overprint (LCT) that was removed during the AF steps (up to 12 mT) and during thermal steps below 200°C. Prior to any structural corrections, and regardless of site lithology, these components mostly aligned within α95% confidence with the present-day magnetic field direction in the study location (see Figure S7 in Supporting Information S1). The LCT components are therefore interpreted as a recent overprint, likely due to viscous remanent magnetization (VRM) (Pullaiah et al., 1975).

Most of the sedimentary sites (SA02, SA04–SA11, SA14, SA20, and SA23) exhibited two high temperature components (see Figure 4). Components with unblocking temperatures consistent with magnetite and titanomagnetite were isolated in thermal demagnetization steps between 450 and 580°C (HT1), and components with unblocking temperatures consistent with hematite or titanohematite were isolated in thermal demagnetization steps between 640 and 680°C (HT2). A subset of the sedimentary sites (SA03, SA12, SA13, SA15, and SA16) had HT1 components, but no HT2 components. Based on the presence of rounded detrital magnetite/titanomagnetite grains in the sedimentary samples (see Figure S4 in Supporting Information S1) and a geomagnetic polarity reversal (see below and Figure 2) we interpret HT1 as a detrital remanence (DRM) that was acquired near to the time of deposition. The HT2 components had similar directions as HT1 in most sedimentary samples, often with a slightly shallower inclination in tilt-corrected coordinates. The HT2 components could represent a hematite DRM which typically has shallower inclination than magnetite DRM due to the platy shape of detrital hematite grains. However, in some samples the HT2 components had a different declination to the HT1 direction, suggesting that some of the HT2 components may also have been acquired after deposition. The absence of HT1 in sites SA22 and SA03 suggests either that there is only detrital hematite in the sample or that any magnetite in the site has been altered to hematite/titanohematite. Given the uncertainty in the origin of the HT2 magnetization in our sedimentary samples, we only used HT1 components to determine the mean paleomagnetic pole. Sedimentary sites that yielded only HT2 magnetizations (SA03 and SA22) were therefore excluded.

Two sites (SA17 and SA18) had components consistent with titanomagnetite that were isolated between 450 and 550°C (HT1) and antipodally directed components with unblocking temperatures between 300 and 400°C (LT). These antipodally directed components may be the result of self-reversal properties of titanomagnetite during alteration intergrowth with titanohematite that is sometimes observed in sedimentary paleomagnetic samples (Garming et al., 2007; Sprain et al., 2016). Samples from site SA19 had only LCT components and no high-temperature components and samples from SA09 had LCT components but became highly unstable at temperatures exceeding 640°C and were excluded from further analysis. Samples from sites SA13, SA14, SA20, and SA21 were excluded because the high temperature magnetization directions from these samples were not sufficiently clustered to achieve a site mean with $n > 5$ and directional uncertainty of $\alpha_{95} < 15°$ (Van der Voo, 1990).

Sites SA24–SA34 comprise lava flows interbedded with the sedimentary strata and are of primarily andesitic composition with the exception of SA26 which is a welded ignimbrite. Sites SA30–SA34 from the top of the volcanic pile exhibited no high-temperature magnetization components and so are likely dominated by multi-domain grains susceptible to VRM overprint. The LCT components of these sites aligned within error of the present-day field direction (see Figure S7 in Supporting Information S1). In addition to LCT components with the same direction and unblocking temperature range and direction as the other sedimentary and volcanic samples, sites SA24–SA29 exhibited high-temperature magnetization components with unblocking temperatures consistent with magnetite/titanomagnetite that were isolated in thermal demagnetization steps between 540

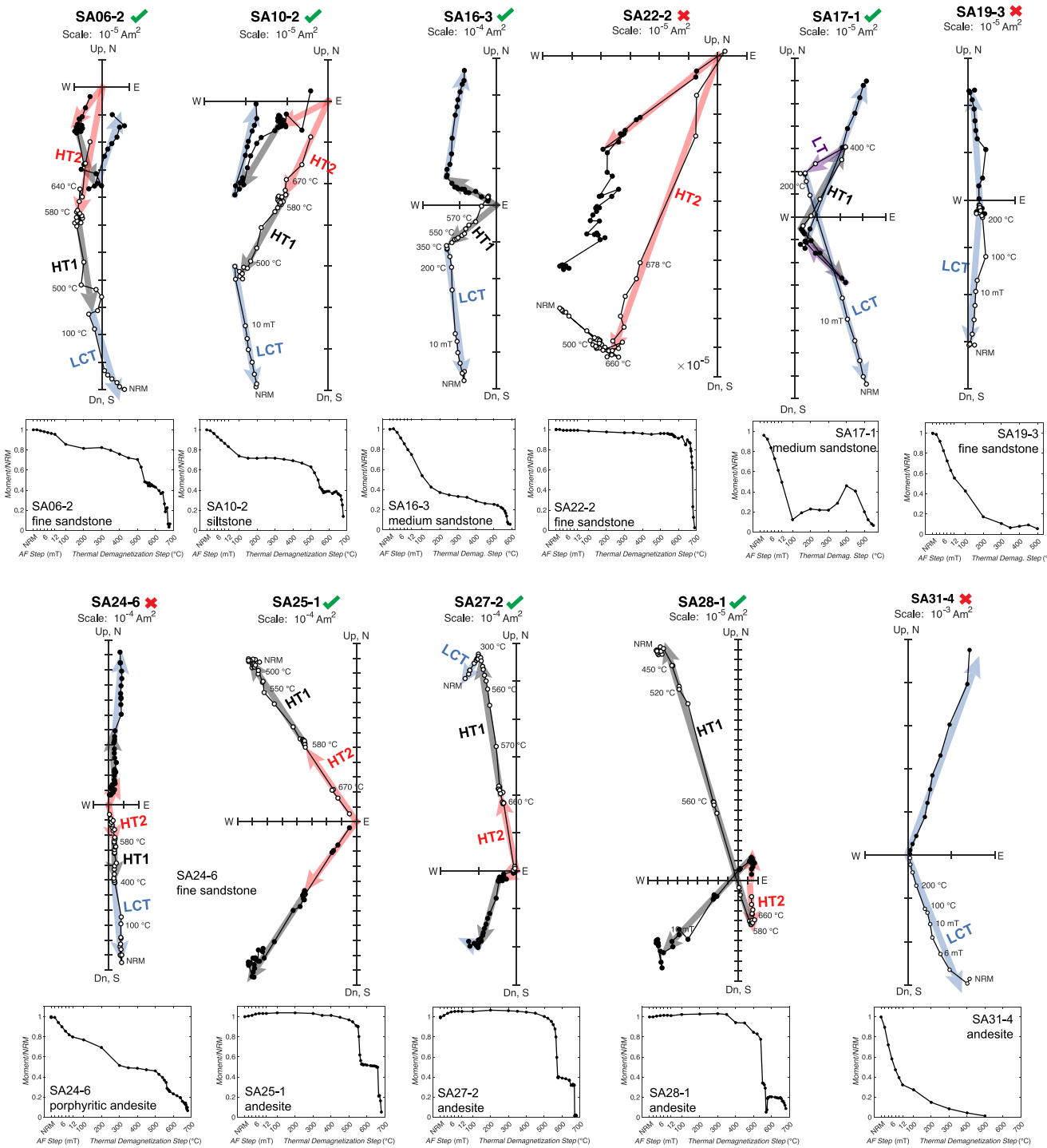

Figure 4. Orthographic projection diagrams and relative moment magnitude decay plots showing alternating field and thermal demagnetization data from a suite of representative samples. The rock type of each sample is labeled on the moment decay diagrams, the top row of diagrams shows demagnetization data from sedimentary rock samples, the bottom row shows demagnetization data from volcanic rock samples. Data are presented in geographic coordinates; closed symbols represent north–south–east–west projections, and open symbols represent up–down–east–west projections. Interpretations are shown with colored arrows: each arrow reflects a direction vector corresponding to components inferred from principal component analysis. Low coercivity and low temperature overprint (LCT) are shown with blue arrows, low temperature overprint (LT) are shown with purple arrows, high temperature components associated with magnetite/titanomagnetite (HT1) are shown with black arrows and high temperature components associated with titnanohematite or hematite (HT2) are shown with red arrows. The magnetic components used to determine the characteristic remanent magnetization of the samples are the HT1 components carried by magnetite/titanomagnetite. Samples that yielded high-temperature magnetization components that were acceptable for further analyses are marked with a green tick mark and samples that were rejected from the study are marked with red crosses.

and 580°C (HT1). The euhedral magnetite/titanomagnetite grains observed in these samples (see Figure S4 in Supporting Information S1) and the fact that the HT1 components from andesite clasts pass a conglomerate test (see below and Figure 5h) suggests that HT1 represents a primary thermoremanent magnetization (TRM) during cooling of the volcanic flows. All the volcanic sites except SA29–SA34 also contained components with unblocking temperatures consistent with hematite/titanohematite that were isolated between 620 and 680°C (HT2). In these samples, hematite/titanohematite mantles and overgrows magnetite grains (see Figure S4 in Supporting Information S1) so the HT2 components are strictly speaking secondary. However, the HT2 directions were almost always parallel to HT1 and they also pass the conglomerate test (see below and Figure 5h). This suggests that HT2 was acquired very shortly after eruption, likely as a result of deuteric auto-alteration. Unlike the other volcanic sites, in site SA28 the HT2 components are antipodal to HT1, this could be the result of self-reversal during titanohematite and titanomagnetite intergrowth or a partial overprint due to alteration before tilting at a time of different magnetic polarity. In any case, for both the volcanic and sedimentary samples we selected the HT1 components as the characteristic remanent magnetization (ChRM) to be used in subsequent calculation of the paleomagnetic pole for the Saltoro Formation. This determination was based on the strong evidence for their primary acquisition (textural observations, reversals, conglomerate test).

To conclusively test whether the high temperature magnetization components (both HT1 and HT2) exhibited by our volcanic samples reflects the orientation of Earth's magnetic field at the time the rocks formed, we conducted a conglomerate test on specimens from 30 primarily andesitic clasts in a cobble-conglomerate unit (site SA01) near the base of the sampled section (see Figure 5h). The magnetization directions of large transported sedimentary clasts in a conglomerate should be randomly distributed when they are deposited, whereas a magnetic overprint would produce clast magnetization directions aligning to the magnetic field at the time of overprinting (i.e., not randomly distributed) (Van der Voo, 1990). We performed a Watson test to determine whether the magnetization directions of both HT1 and HT2 components from the clasts in site SA01 were randomly distributed (Watson, 1956). For the suite of clasts with HT1 and HT2 magnetization directions we obtained resultant vectors of $R_{HT1} = 4.33$ and $R_{HT2} = 3.18$ respectively. Since R_{HT1} and R_{HT2} are both less than the critical value of $R_0 = 8.80$ for $N = 30$ directions, we cannot rule out the null hypothesis that the magnetization directions are randomly distributed with 95% confidence. The conglomerate test is therefore successful, indicating that both the HT1 and HT2 high temperature magnetization directions recorded by our volcanic samples have not been overprinted after deposition and support a primary TRM origin for the HT1 components and a deuteric auto-alteration origin for the HT2 components.

Additional strong evidence for the primary origin of HT1 magnetization in the sedimentary sites comes from directions from sites SA17 and SA18 that are antipodally reversed compared to those from sites SA16 and the underlying stratigraphy. These sites define a reversal of Earth's geodynamo situated at the expected stratigraphic location for the C34n to C34r reversal at 83.65 Ma (see Figure 2) (Gradstein et al., 2020). Sample LB19-06 was collected from 160 m up section of the reversal and its depositional age is within error of the reversal age suggesting that our age determinations fall very close to the true maximum depositional ages of the sandstones sampled throughout the Saltoro section. After inclination shallowing (E/I) and vertical axis rotation (VAR) corrections (see below), the normal and reversed populations pass a bootstrap reversal test (Tauxe, 2010) demonstrating that they are indeed antipodally reversed (see Figure S8 in Supporting Information S1). The presence of a magnetic reversal in the stratigraphy in the expected location is strong evidence for primary magnetization because a regional magnetic overprinting event would have obliterated the reversal record, remagnetizing all samples to the same polarity (Van der Voo, 1990). Furthermore, the successful reversal test rules out even a partial remagnetization of the ChRM directions (Tauxe, 2020). Any partial overprint that affected the Saltoro Formation was removed by excluding HT2 directions from our study. One other normal polarity magnetochron (C33n) is expected within the sampled stratigraphic section between LB19-58 and LB19-56 (Gradstein et al., 2020), however, it is not present in our paleomagnetic results because there are no sites in this interval.

To identify and correct for possible compaction related shallowing of inclination in our sedimentary paleomagnetic data sets, we used the elongation/inclination (E/I) method (Tauxe & Kent, 2004). Application of the E/I method to 96 sedimentary HT1 magnetic directions from accepted sites yielded a flattening factor of $f = 0.57$ with bootstrapped confidence bounds of (0.76, 0.42), which we used to correct the sedimentary site-mean direction data before determination of the paleopole (see Figure 5c and Figure S9 in Supporting Information S1). The E/I correction applied here uses close to the optimum $N \geq 100$ suggested by Tauxe and Kent (2004). The correction modified the mean inclination of uncorrected sedimentary sites from $I_{(uncorrected)} = 23.8 \pm 10.7°$ to an E/I corrected inclination of $I_{(corrected)} = 36.0 \pm 11.5°$ (see Figure 5c). The validity of the E/I correction is bolstered by the fact

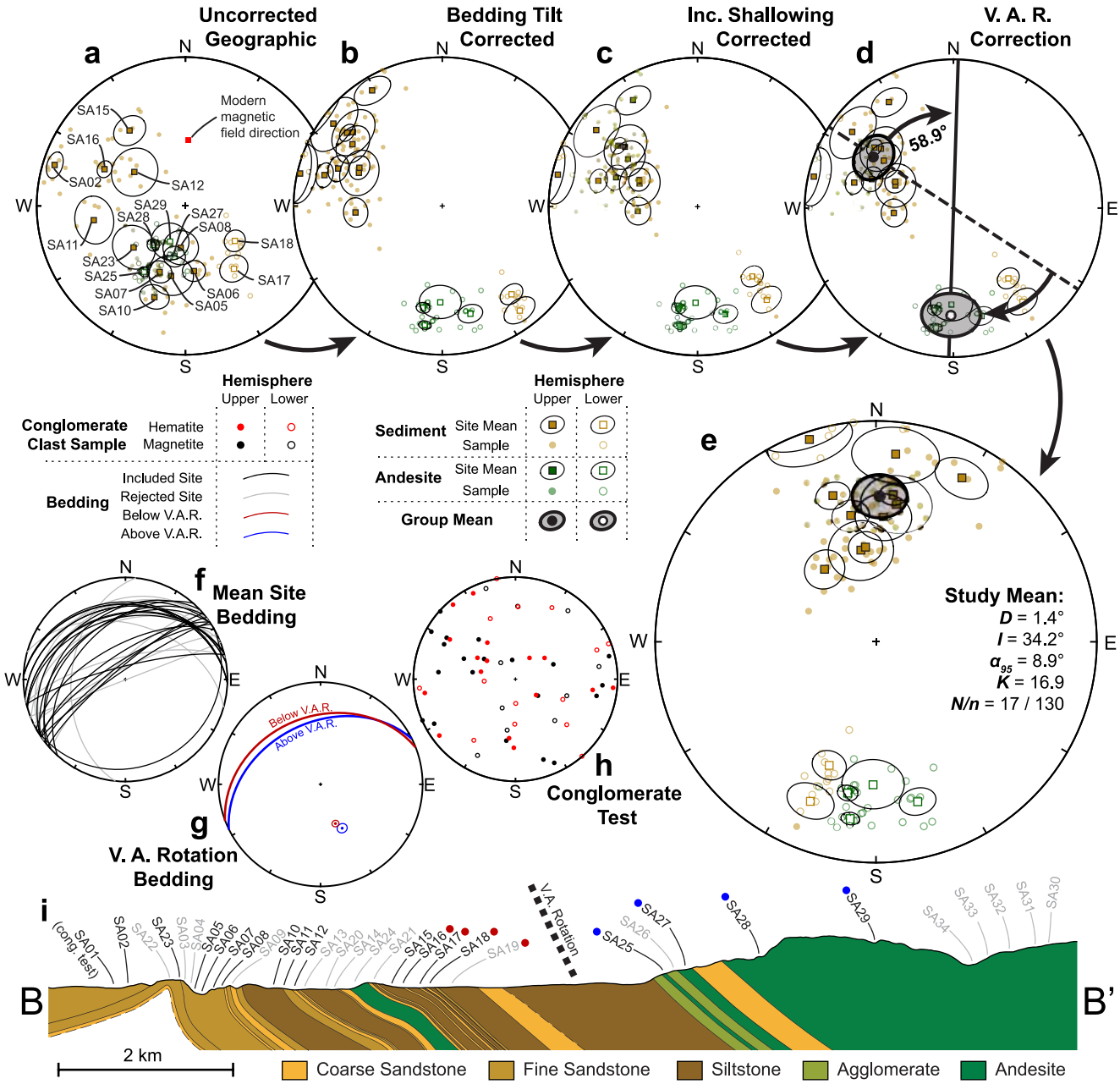

Figure 5. Stereographic projections showing paleomagnetic results from the Saltoro Formation with each panel showing successive corrections that have been applied to the data. Measurements from volcanic samples are shown with green symbols and sedimentary samples with brown symbols, open symbols indicate upper hemisphere projections while filled symbols indicate lower hemisphere projections. Circular symbols represent sample characteristic remanent magnetization (ChRM) directions, square symbols represent site mean ChRM directions with their α_{95} uncertainty displayed as a black ellipse. (a) Paleomagnetic results shown in geographic coordinates. (b) Paleomagnetic results after bedding tilt correction. (c) Paleomagnetic results after sedimentary sites have been corrected for inclination flattening. (d) Means of each sub-population before vertical axis rotation (VAR) correction was applied. (e) Final fully corrected paleomagnetic data set with the study mean direction displayed using a solid black circle symbol and a shaded α_{95} uncertainty ellipse. (f) Stereographic projection of the mean of bedding planes at each site, black lines indicate sites included in the paleomagnetic study and gray lines indicate sites that were excluded. (g) Stereographic projection of the mean of bedding planes from horizons close to the stratigraphic height of the VAR in the paleomagnetic results, with bedding from the rotated stratigraphy shown in blue and bedding from the unrotated stratigraphy shown in red. The bedding is almost identical above and below the rotation, providing strong evidence that the rotation took place along a vertical axis. (h) Magnetization directions associated with magnetite (black symbols) and hematite (red symbols) in samples from conglomerate clasts from near the base of the Saltoro stratigraphy. The random distribution of magnetic directions demonstrates that neither hematite (HT2) nor magnetite (HT1) magnetization in the Saltoro Formation volcanics has been overprinted. (i) Cross-section of the paleomagnetic sampling section with the location of each sampling site marked. Sites that were excluded from the paleomagnetic study are shown in gray and sites that were included are shown in black. The sites from above and below the V.A. rotation interval that were used to make panel (g) are marked with blue and red circles.

that the corrected inclination is within error of the mean inclination of the volcanic sites ($I_{volc.}$ = 28.5 ± 13.8°), which do not require shallowing correction.

After the corrections are applied for bedding tilt and inclination shallowing in sedimentary sites, the site-mean magnetization directions from the Saltoro Formation fall into two groups with distinct mean declinations (see Figure 5d). Sites SA25–SA29 at the top of the sampled stratigraphy have a mean normal-polarity declination of D = 001.4 ± 13.8°, while samples stratigraphically beneath SA25 have a mean normal-polarity declination of D = 302.5 ± 12.1° which we interpret as corresponding to an anti-clockwise VAR of 58.9 ± 25.9° in the stratigraphic interval between sites SA18 and SA25. We considered a number of other possible causes for this rotation including, incorrect structural correction due to either angular unconformity, rotation along an unidentified fault surface or an unidentified plunging fold, and the uppermost volcanic stratigraphy not sampling PSV. The volcanic stratigraphy likely sample PSV because successive volcanic flows also do not share common mean directions, as would be expected if they recorded the same ambient magnetic field. This indicates that they record distinct directions and therefore should be treated as independent spot readings of the magnetic field rather than being averaged together into a group. The volcanic sites are also distributed within a 1,610 m thick succession of volcanic flows and intervening sedimentary horizons that accumulated over millions of years so it is very unlikely they recorded the same instantaneous spot reading of the magnetic field (Deenen et al., 2011). Any type of the structural reorientation process (e.g., fold, fault) would be expected to produce different bedding orientations over the transition between the rotated and unrotated sites. However, the mean bedding orientation across this interval is almost identical (See Figure 5g). The rotation, therefore, must have occurred around a vertical axis during the deposition of the Saltoro Formation rather than during subsequent deformation. This rotation possibly occurred during extension of the Eurasian margin (Karakoram and South Pamir) in the Late Cretaceous (Chapman et al., 2018b). It is also important to note that the VAR in our data has no effect our E/I flattening correction. Accurate determination of the flattening factor using the E/I method relies on the assumption that there are no sources of scatter within the data other than paleo-secular variation (PSV) of the geodynamo (Vaes et al., 2021). Since all of the sedimentary sites are situated in the rotated lower portion of the stratigraphy, there is no differential rotation between the sedimentary sites and no effect on the shallowing correction.

After a correction was made for the VAR, northern hemisphere virtual geomagnetic poles (VGP) were used to determine the paleopole. VGPs are more likely to have a Fisher distribution than site-mean paleomagnetic directions (Deenen et al., 2011). The time-averaged mean paleomagnetic pole for the Saltoro Formation is situated at P_{Lon} = 254.7°E and P_{Lat} = 75.2°N with a 95% uncertainty bound of A_{95} = 8.9° and precision parameter K = 19.8. The corresponding paleolatitude of the Saltoro Formation is 19.9 ± 8.9°N in the time period between 92.9 ± 2.2 and 74.6 ± 0.7 Ma (see Figure 6). The same latitude is obtained using the data set before V.A.R. correction (21.8 ± 14.2°N), albeit with larger uncertainty due to the wider declination range produced by the uncorrected rotation.

We compared the Saltoro Formation paleopole to well-established reliability criteria to determine paleopole reliability and it meets all the applicable criteria (Meert et al., 2020; Van der Voo, 1990). The Saltoro Formation paleopole has a very well constrained U/Pb zircon age and the >18.3 million years spanned by the Saltoro stratigraphy is easily long enough to achieve appropriate sampling of PSV of the geodynamo, and the A_{95} uncertainty for the Saltoro Formation paleopole is comfortably within the acceptable range to reliably average PSV of the geodynamo (13.8° ≥ A_{95} ≥ 3.9° for N = 17) defined by Deenen et al. (2014). The number of samples used to calculate the paleopole (n = 130) exceeds the minimum criterion of n ≥ 25, the precision parameter (K = 19.8) is in the range 70 ≥ K ≥ 10, and number of sites (N = 17) is well above the required threshold of N ≥ 8 (Deenen et al., 2014; Meert et al., 2020). The separation of the natural remanent magnetization into constituent components was achieved using modern demagnetization techniques. The magnetic carriers were constrained with rock magnetic analyses and microscopy. There is good structural control and inclination shallowing of sedimentary data was corrected using the E/I method. Finally, a primary origin of remanence was confirmed by both a successful conglomerate test and the presence of a geomagnetic reversal at the expected stratigraphic level that passes a bootstrap reversal test. Overall, this suggests that the paleomagnetic pole that we obtained from the Saltoro Formation is of high reliability and can be used in paleomagnetic reconstructions with confidence.

5. Discussion

5.1. Age of the Shyok Suture Zone

Our results from the Saltoro Formation constrain the paleolatitude of the Karakoram terrane to 19.9 ± 8.9°N at 92.9–74.6 Ma. This latitude is significantly different from that of the KLA, which is constrained by paleomagnetic

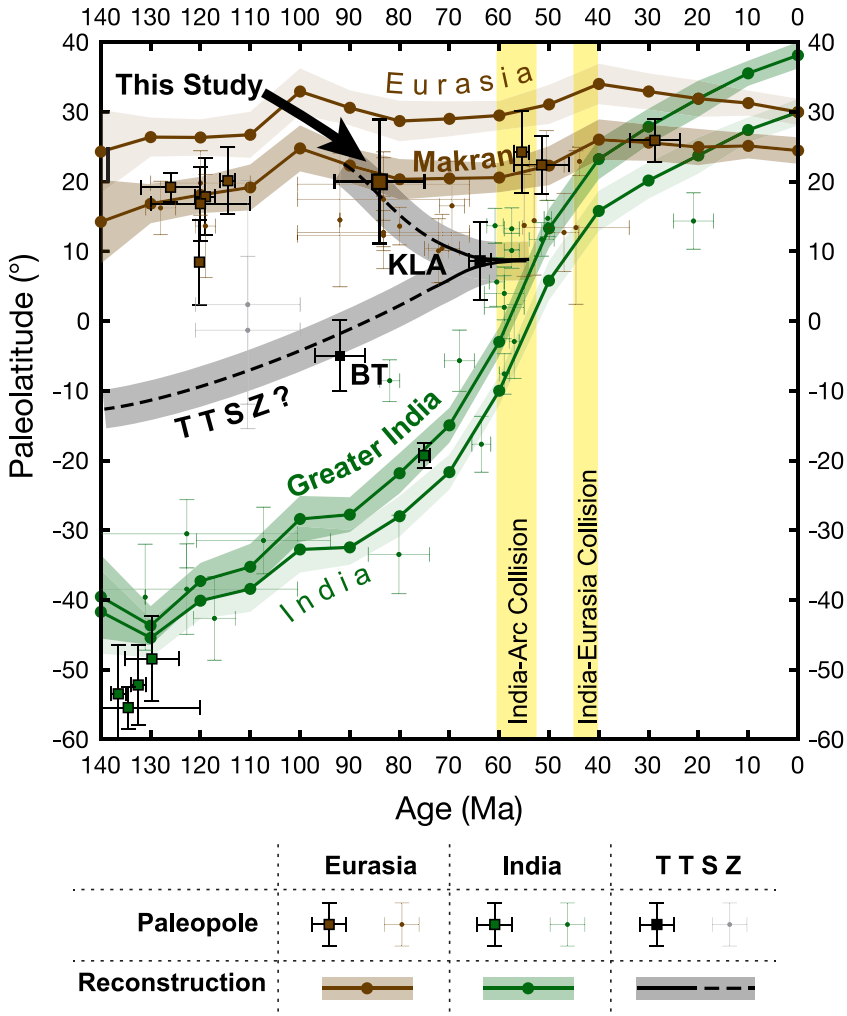

Figure 6. Plot of paleolatitude against age showing reconstructed motions of India (green) and Eurasia (brown) along with all the available paleomagnetic constraints from the Tethys Himalaya (green) and Eurasian margin terranes (brown) and the Kohistan-Ladakh arc (KLA) and Burma Terrane intra-oceanic arc remnants (gray/black). The most robust paleopoles are shown with square symbols and less reliable poles are shown with small circle symbols. The lowermost curve labeled "India" is the calculated position of the study site (34.6°N, 77.5°E), if it moved rigidly in its present-day geometry relative to India. The uppermost curve labeled "Eurasia" is the calculated position of the study site if it moved rigidly in its present-day geometry relative to Eurasia. The curve labeled "Makran" is shown for comparison because Makran is part of the modern southern Eurasian margin that was minimally affected by India-Eurasia collision at the resolution of paleomagnetic data. The curve labeled "Greater India" shows the paleolatitude of a theoretical point in north-central Greater India based on an assumed linear northern margin of Gondwana between Arabia and northern Australia (Ali & Aitchison, 2005). The reference locations used to calculate the paleolatitude of Makran and Greater India are shown on the first panel of Figure 7. The black curves with gray shading show two possible models for the paleolatitude of the KLA. The upper dashed black line reflects the scenario in which the KLA formed proximal to or part of the southern Eurasian margin before ~93 Ma and subsequently rifted southward to its Paleocene latitude. The lower dashed black line reflects the possible position of the KLA if it formed independently of the Eurasian margin as part of the Trans-Tethyan Subduction Zone (TTSZ).

results from the Khardung volcanics to a paleolatitude of 8.1 ± 5.6°N between 66.1–61.6 Ma (Martin et al., 2020). These results conflict with a postulated Late Cretaceous (85–93 Ma) closure age of the Shyok suture (Borneman et al., 2015; Gaetani et al., 1993; Petterson & Windley, 1985). If the Khardung Formation formed after the accretion of the KLA to Eurasia and closure of the Shyok suture (Pundir et al., 2020; Saktura, Buckman, Aitchison, & Zhou, 2021), then their paleopole and paleolatitude would be indistinguishable from that of the Saltoro Formation. Instead, the Saltoro Formation and Khardung Formations do not share a common paleopole indicating that the KLA and Eurasian forearc had not converged at the time of Khardung volcanics eruption. This places a maximum age limit of <61.6 Ma for final closure of the Shyok suture zone, derived from the <61.636 ± 0.11 Ma

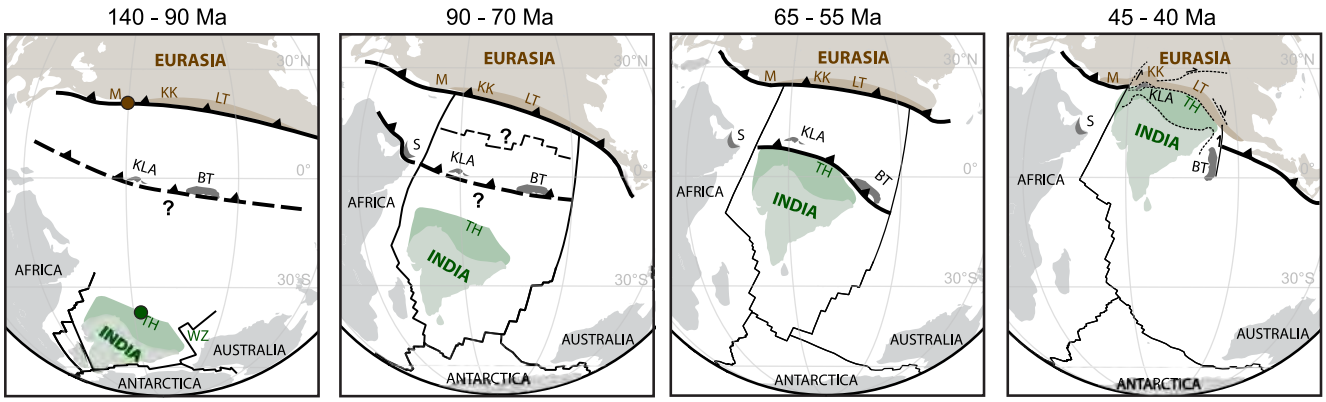

Figure 7. Reconstructions of the Neotethys Ocean based on only the most robust paleomagnetic data for four time periods since the Early Cretaceous. Divergent and transverse plate boundaries are shown with solid black lines, and subduction zones are displayed with thick lines with triangular ticks indicating the direction of subduction and dashed lines where the paleogeography is poorly constrained. Major terranes and relevant locations are indicated with letter codes: BT = Burma terrane, KK = Karakoram terrane, KLA = Kohistan-Ladakh arc, LT = Lhasa terrane, M = Makran, S = Semail ophiolite (Oman), TH = Tethyan Himalaya, and WZ = Wallaby-Zenith Fracture Zone. The reference locations used to calculate the paleolatitude of Makran and Greater India in Figure 6 are shown on the first panel with a dark green circle (for Greater India after Ali and Aitchison (2005)) and a brown circle for Makran.

CA-ID-TIMS zircon age bracketing the Khardung volcanics paleopole (Martin et al., 2020). This age estimate is likely conservatively old since two of the paleomagnetic sites from Martin et al. (2020) are from stratigraphically above their youngest age. The Khardung volcanics strata above the Martin et al. (2020) sample section is dated to 51.9 ± 0.7 Ma (Saktura, Buckman, Aitchison, & Zhou, 2021). The difference in the paleopoles is substantiated by a common mean test (Tauxe et al., 1991) performed using the VGP distributions of both the Khardung volcanics and the Saltoro Formation which demonstrates with 95% certainty that the paleomagnetic data sets define different paleopoles (See Figure S10 in Supporting Information S1). The paleopole comparison is also unaffected by the challenges associated with comparing individual study mean paleomagnetic poles to a reference pole from an apparent polar wander path (APWP) that was recently highlighted by Rowley (2019) because it derives from the direct comparison of two paleopoles from nearby locations.

A post-61.6 Ma age for the Shyok suture zone is consistent with early studies that interpreted that the Shyok suture zone closed in the Eocene-Oligocene (Andrews-Speed & Brookfield, 1982; Brookfield & Reynolds, 1981; Sharma, 1987). This early interpretation was unfortunately abandoned when Petterson and Windley (1985) posited that the SSZ formed in the Late Cretaceous (85–104 Ma) based on the Rb-Sr whole rock ages of granitoids and the presence or absence of a pervasive gneissic fabric (i.e., younger intrusions undeformed, older deformed). However, Jagoutz et al. (2009) demonstrated using modern U-Pb zircon ages that no relationship exists between the presence or absence of gneissic fabric and the intrusion age of felsic plutons in Kohistan.

The young age of the Shyok suture zone was further obfuscated by Borneman et al. (2015), who suggested a 92–85 Ma age based on the depositional age of the Eurasia-derived Saltoro Formation sedimentary rocks and the 85.2 ± 3.8 Ma U-Pb zircon age of a felsic dike crosscutting what they interpreted as an unconformity between Saltoro Formation and the Shyok volcanics. Contrary to previous work interpreting the Shyok volcanics and Saltoro Formation as part of the southern margin of Eurasia (Rai, 1982; Sharma, 1987; Thanh et al., 2012), they asserted that the Shyok volcanics and Saltoro Formation were part of the KLA and interpreted the presence of Eurasia-derived zircons in the Saltoro Formation as an age constraint for the KLA-Eurasia collision. Additionally, the dike dated by Borneman et al. (2015) does not crosscut a Shyok/Saltoro unconformity as postulated, but rather an angular unconformity within the Saltoro Formation in which clastic sedimentary rocks are deposited on one of the many andesitic volcanic flows that are common within the Saltoro stratigraphy (see Figure S1 in Supporting Information S1). Borneman et al. (2015) interpreted that the Saltoro fault becomes an unconformity along strike. However, within the study area of Borneman et al. (2015), the Saltoro fault is spectacularly exposed at a lower structural level separating the Saltoro Formation andesites, agglomerates and sedimentary rocks from typical pillow basalts of the Shyok volcanics (see Figure 1b; Figure S1 in Supporting Information S1). Thus, the rationale for the Late Cretaceous formation age of the Shyok suture zone proposed by Borneman et al. (2015) is not supported by the field relationships.

Indeed, the angular unconformity referred to by Borneman et al. (2015) is associated with syn-sedimentary normal faulting (see Figure S1 in Supporting Information S1), suggesting that the Karakoram margin was

undergoing extension and subsidence at around 93–83 Ma, not compressional orogenesis. The anti-clockwise VAR of the Saltoro stratigraphy in our paleomagnetic results also occurred at ∼83 Ma, so may be related to this extension. Late Cretaceous Karakoram extension may also explain the angular unconformity in northern Pakistan where deformed Jurassic strata of the Karakoram block are overlain by subaerial alluvial fan deposits that are onlapped by Campanian (83.6–72.1 Ma) marine wackestones and mudstones (Tupop Fm. and Durband Fm.; Gaetani et al., 1993). Cretaceous extension along the Karakoram margin is consistent with the magmatic evolution of the Karakoram and south Pamir which has been recently interpreted to suggest extension between 80 and 70 Ma due to Neotethyan slab rollback (Chapman et al., 2018b). It is also consistent with the postulated back-arc extension and rifting of the Xigaze forearc southward from Eurasia due to a retreating subduction zone (Kapp & DeCelles, 2019; their Scenario 2). Southward rifting of the Eurasian margin could provide an additional mechanism for delivering Eurasian derived sediments to the Indian margin during a Paleocene India-arc collision (An et al., 2021; DeCelles et al., 2014; Najman et al., 2017) without requiring full closure of the Neotethys Ocean.

The difference in age between our paleomagnetic results and those of Martin et al. (2020) leaves open the possibility that the Karakoram terrane moved southward toward the KLA between 75 and 66 Ma, resulting in a >61.6 Ma closure of the Shyok suture zone. However, the absence of a younger suture zone north of the Shyok suture zone makes this scenario unlikely. Furthermore, this southward motion of the Karakoram block relative to Eurasia would be required to occur at a rapid ∼14 cm/yr and is not supported by paleomagnetic evidence from the Lhasa terrane which indicates that the Eurasian margin remained at a stationary paleolatitude of ∼18–22°N from the Early Cretaceous until the Eocene (Lippert et al., 2014; van Hinsbergen et al., 2019).

In summary, both geologic and paleomagnetic records suggest that the final closure of the Shyok suture zone occurred in the Paleogene, after 61.6 Ma, and most likely in the Eocene at around 45–40 Ma as constrained by the appearance of an evolved crustal signature in the ε_{Hf}, ε_{Nd} and $^{87}Sr/^{86}Sr$ isotopic record of KLA magmas at 40.4 ± 1.3 Ma (Bouilhol et al., 2013). This conclusion is independent of whether the KLA moved southward to its Paleocene latitude from the Eurasian margin due to slab rollback and opening of a back-arc basin after 93 Ma, or if it formed above a long-lived intra-oceanic subduction zone outboard of the Eurasian margin. An Eocene final collision is also consistent with the age of migmatization, leucogranite emplacement, and deformation in response to a continental collision at 45–40 Ma (Aikman et al., 2008; Burg & Bouilhol, 2019; Cowgill et al., 2003; Leloup et al., 2001; Yin et al., 1999). In addition, crustal shortening estimates from across Tibet and the Himalayan fold and thrust belt are in better agreement with the amount of India-Eurasia convergence that occurred after 40 Ma (DeCelles et al., 2002; Martin et al., 2020; van Hinsbergen et al., 2011).

5.2. Paleomagnetic Reconstruction of the Neotethys

Reconciling the various conflicting India-Eurasia collision models relies on a robust understanding of the relative positions of the leading edge of India, the KLA and any other trans-Tethyan subduction system remnants, and the southern margin of Eurasia through time. Our results represent the only Cretaceous paleomagnetic constraint from the Karakoram terrane and so provide an important constraint on the location of the Eurasian margin in the western extent of the belt. They suggest that the Karakoram terrane was situated at a comparable latitude to other elements of the Eurasian margin including the Lhasa and Qiangtang blocks and therefore comprised a contiguous element of the southern Eurasian continental margin in the Campanian. To aid the discussion of our results in the broader context of the paleo-reconstructions of India, the Trans-Tethyan-subduction system, and Eurasia we will review paleomagnetic constraints from each of the three tectonic plates, and then synthetize the results to derive the tectonic evolution of the Neotethyan realm. The compilation of paleomagnetic poles for our synthesis is presented in Table S6 in Supporting Information S2.

5.2.1. Paleomagnetic Constraints on Eurasia

The most reliable paleomagnetic data show that the Lhasa terrane was situated at a constant ∼18–22°N latitude from the Early Cretaceous until the Eocene, throughout the closure of the Neotethys ocean (Dupont-Nivet et al., 2010; Lippert et al., 2014; van Hinsbergen et al., 2019). Reliable Cretaceous paleomagnetic results from volcanic and sedimentary successions across Tibet yield paleolatitudes around 16–20°N (Bian et al., 2017; W. Chen et al., 2012; Li et al., 2017; Ma et al., 2014, 2017; Yang et al., 2015b). The majority of Late-Cretaceous to Eocene paleomagnetic data are derived from the Eocene Linzizong volcanics and underlying Cretaceous sedimentary strata that are well exposed in the Linzhou area near Lhasa in eastern Tibet. Paleomagnetic studies of these units have yielded a large range of paleolatitudes between 5°N and 24°N (Achache et al., 1984; Cao

et al., 2017; J. Chen et al., 2010, 2014; Dupont-Nivet et al., 2010; Liebke et al., 2010; Lippert et al., 2014; Sun et al., 2010, 2012; Tan et al., 2010; Tong et al., 2022; Yi et al., 2021). However, careful paleomagnetic and rock magnetic analyses have demonstrated that the spread in paleolatitudes is the result of a low-latitude bias caused by a combination of uncorrected inclination shallowing in sedimentary sites and partial remagnetization after tilting (Huang et al., 2013, 2015). Lippert et al. (2014) rigorously filtered Linzizong volcanic data to mitigate these effects and their analysis yielded an Eocene paleolatitude of 21.1 ± 4.1°N between 56–47 Ma (for a reference location on the Yarlung-Tsangpo suture zone at 29.0°N and 88.0°E). The only other Eocene constraints on the Lhasa Terrane are from the Xigaze forearc basin exposed near Zedong in west-central Tibet, which yield a paleolatitude of 24.2 ± 5.9°N between 57 and 54 Ma (Meng et al., 2012; Tong et al., 2022). These results are consistent with those of Lippert et al. (2014), although the data sets have significant scatter and have not been corrected for inclination shallowing.

The reliable paleomagnetic record from across the southern Eurasian margin, including our results, are in very close agreement with the paleolatitude of Makran, part of the Eurasian margin minimally affected by collision, that was reconstructed using the Eurasian APWP of Torsvik et al. (2012) (See Figures 6 and 7). Since Makran is part of the present day southern Eurasian margin in Iran, where effects related to the Indian-Eurasia collision are relatively minor (at least at the uncertainty level of paleomagnetic data), its restored paleolatitude provides a reasonable approximation of the pre-collisional Eurasian margin eastward into the Karakoram and Tibet.

5.2.2. Paleomagnetic Constraints on Greater India

Owing to the dearth of volcanic rocks that are considered the optimum target for paleomagnetism, and the widespread thermal and chemical overprint in the Tethys Himalaya sedimentary rocks (Appel et al., 2012; Crouzet et al., 2003; Dannemann et al., 2022; Huang et al., 2017; Schill et al., 2002; Xu et al., 2022), the location of the northern edge of Greater India is more challenging to constrain than the Eurasian margin. Results from Paleocene limestones of the Tingri and Zongpu Formations were originally interpreted to suggest the Tethys Himalaya was situated 2,000–3,000 km north of cratonic India at the onset of collision (Besse et al., 1984; Patzelt et al., 1996; Tong et al., 2008; Yi et al., 2011), but these successions have since been shown to be remagnetized (Huang et al., 2017; Liebke et al., 2013).

The best paleomagnetic data from the northern Indian margin derive from basaltic flows that were erupted between 140 and 125 Ma, while India was still proximal to Gondwana (Bian et al., 2019; Ma et al., 2016; Yang et al., 2015a). Although these represent valuable constraints on Indian plate motion, they are of limited utility in constraining the size of Greater India in the runup to collision due to the significant rotation of India since Gondwana breakup (Zhang & Huang, 2017).

Recent, high quality paleomagnetic data from 76 to 74 Ma shales in south-central Tibet suggest that the Tethyan Himalaya was situated at a paleolatitude 19.4 ± 1.8°S, suggesting Greater India had a latitudinal extent of 715 ± 374 km (Yuan et al., 2021, 2022). Yuan et al. (2021, 2022) also obtained a 62.5–59.2 Ma paleomagnetic pole from clastic successions at Mulbala and Sangdanlin with a paleolatitude of 14.1 ± 1.9°N, suggesting a western Greater India extent of 1,342 ± 484 km, leading them to revise the timing of van Hinsbergen et al. (2012)'s Greater India basin rifting model to involve rifting of the Tethyan Himalaya northward between 74 and 63 Ma. This paleolatitude is slightly north of the 8.1 ± 5.6°N of the KLA at 66–61 Ma (Martin et al., 2020) suggesting convergence between Greater India and the KLA in the Paleocene (Yuan et al., 2022). In the absence of geologic evidence for a Greater India basin and rifting of northern India between 74 and 63 Ma (Searle, 2019), more constraints are needed to substantiate the extent to which the inferred extension is real or an artifact of the rapid motion of India in the Paleocene and the inherent scatter in paleomagnetic data. Reconstructing Greater India based on the Wallaby-Zenith Fracture zone off western Australia and the fit of India into Gondwana (Ali & Aitchison, 2005), predicts paleolatitudes of the Tethyan Himalaya that are in agreement with the reliable paleomagnetic data (see Figure 6).

5.2.3. Paleomagnetic Constraints on the KLA

The only reliable paleomagnetic constraint on the position of the KLA is the 8.1 ± 5.6°N paleolatitude of the Khardung volcanics reported by Martin et al. (2020). The paleomagnetic record is presently unable to resolve the paleogeography of the KLA prior to 66 Ma because paleomagnetic studies from Cretaceous rocks from Kohistan either yielded overprinted remanences (Ahmad et al., 2000, 2001), or fall short of modern reliability standards (Klootwijk et al., 1979, 1984; Zaman & Torii, 1999; Zaman et al., 2013). This leaves open the

possibility that the KLA formed near to or collided with the Eurasian margin before ~93 Ma and subsequently rifted southward to a near equatorial latitude (creating a back-arc basin comparable to the present-day Sea of Japan) before collision with India in the Paleocene (Kapp & DeCelles, 2019; Rolland et al., 2002). Alternatively, the KLA could have formed part of a long-lived intra-oceanic subduction system (similar to the present-day Isu-Bonin-Mariana arc) operational outboard of the Eurasian margin throughout the closure of the Neotethys since ~156 Ma (Jagoutz et al., 2015, 2019). These two possible scenarios are shown with black dashed lines on Figure 6.

In addition to the KLA, the Burma Terrane (BT) that separates India from the Eurasian Sibumasu block (see Figure 1a), has also been proposed to be part of a trans-Tethyan intra-oceanic subduction zone south of the Eurasian margin (Licht et al., 2020; Westerweel et al., 2019). Westerweel et al. (2019) concluded that this terrane was situated at a latitude of 5.0 ± 4.7°S between 97 and 87 Ma and was subsequently rotated into its present-day orientation due to Paleocene collision with the northeast corner of India.

5.2.4. Synthesis

The most reliable paleomagnetic data from the Lhasa terrane show that it remained at around 18°N–22°N between 140–40 Ma throughout the closure of the Neotethys ocean (van Hinsbergen et al., 2019). Our results and analysis of the available paleomagnetic constraints shows that the Karakoram terrane was a constituent part of the Eurasian margin at 19.9 ± 8.9°N in the Campanian and that the Karakoram and KLA had significantly different latitudes at 66.1–61.6 Ma when geologic evidence from the Indian margin records the onset of collision (Beck et al., 1995; Tapponnier et al., 1981). Reliable paleomagnetic data from the Tethyan Himalaya show that the northern edge of India was situated far south of Eurasia at ~8–14°N (Yuan et al., 2021, 2022) at a comparable latitude to the KLA (Martin et al., 2020) at this time. The robust paleomagnetic records of the Himalaya are therefore consistent with the India-arc accretion model for the India-Eurasia collision (see Figure 7). Future paleomagnetic work will establish the pre-Paleocene paleogeography of the KLA and the BT and determine whether they are relics of a long-lived intra-oceanic subduction zone in the Neotethys (Jagoutz et al., 2015) or the product of a rifted back-arc derived from or connected along-strike with the Eurasian margin (Kapp & DeCelles, 2019).

6. Conclusion

Determining in the age of final closure of the Shyok suture zone has been a crucial challenge in evaluating the multiple conflicting tectonic models for the India-Eurasia collision. Our results resolve this challenge by providing an independent paleomagnetic upper bound on the final closure of the Shyok suture zone at <61.6 Ma. These data constrain the Karakoram terrane to a paleolatitude of 19.9 ± 8.9°N between 93 and 75 Ma, comparable to that of the Lhasa and Qiangtang blocks, indicating that the Karakoram terrane formed part of the southern Eurasian margin in the Late Cretaceous (Zanchi et al., 2000). Our results, compared to the results of Martin et al. (2020), suggest that there was a significant oceanic plate or back-arc basin separating the KLA from Eurasia in the Late Cretaceous. Regardless of whether the KLA originated on or near the Eurasian margin and rifted southward after 93 Ma, or developed as part of a long-lived intra-oceanic subduction zone near the equator, a multi-stage arc-continent collision model is required to explain the geological observations and paleomagnetic results from the Shyok suture zone (See Figure 6). The obduction of ophiolites onto northern India at 60–65 Ma (Beck et al., 1995; Tapponnier et al., 1981) and the delivery of arc-detritus to the Indian passive margin strata at 54–52 Ma (Najman et al., 2017) occurred during arc-continent collision between the KLA and India prior to final India-Eurasia collision (Aitchison et al., 2000; Bouilhol et al., 2013; Jagoutz et al., 2015). The final India-Eurasia continental collision in the western part of the orogenic belt occurred along the Shyok suture zone, probably at 45–40 Ma (Bouilhol et al., 2013).

Data Availability Statement

The complete data set of all thermal demagnetization experiments conducted as part of this research are available at Dryad (Martin et al., 2023, https://doi.org/10.5061/dryad.ffbg79d0w link: https://datadryad.org/stash/share/cpV8DUZ2Aleg26xAZiewbtxOKg99H3VdB4M458TV4Ys, which can be viewed and interpreted using the PmagPy software package (Tauxe et al., 2016).

Acknowledgments
We thank Megan Guenther, Santosh Joshi, Abhay-Jeet Joshi, Zoe Levitt, Kate Pryzdzial, Diwakar Bawari, and Jigyasha Bisht for field assistance; C. P. Dorjay for logistical assistance and Nerpa guest-house for the hospitality they provided us in Charasa village, Ladakh. We also thank Jay Shah, and Eduardo Lima for assistance with paleomagnetic and rock magnetic experiments at the MIT Paleomagnetism Laboratory and MIT Ross Laboratory; Jacob Setera, Laura C. Mulrooney, and George Kamenov for assistance with LA-ICPMS analyses at Rutgers University and at University of Florida; Neel Chatterjee for assistance in the MIT Electron Microprobe Facility and Max Brown at the Institute for Rock Magnetism (IRM) at the University of Minnesota. This work was funded by the National Science Foundation (NSF) under Grant EAR-1902179, financially supported by the AGeS program (NSF Grant EAR-1759200 and EAR-1759353) and also by the MIT International Science and Technology Initiatives India (MISTI India) student travel program.

References

Achache, J., Courtillot, V., & Xiu, Z. Y. (1984). Paleogeographic and tectonic evolution of southern Tibet since middle Cretaceous time: New paleomagnetic data and synthesis. *Journal of Geophysical Research*, *89*(B12), 10311–10339. https://doi.org/10.1029/jb089ib12p10311

Ahmad, M. N., Fujiwara, Y., & Paudel, L. P. (2001). Remagnetization of igneous rocks in Gupis area of Kohistan arc, northern Pakistan. *Earth Planets and Space*, *53*(5), 373–384. https://doi.org/10.1186/bf03352394

Ahmad, M. N., Yoshida, M., & Fujiwara, Y. (2000). Paleomagnetic study of Utror Volcanic Formation: Remagnetizations and postfolding rotations in Utror area, Kohistan arc, northern Pakistan. *Earth Planets and Space*, *52*(6), 425–436. https://doi.org/10.1186/bf03352254

Aikman, A. B., Harrison, T. M., & Lin, D. (2008). Evidence for early (>44 Ma) Himalayan crustal thickening, Tethyan Himalaya, southeastern Tibet. *Earth and Planetary Science Letters*, *274*(1–2), 14–23. https://doi.org/10.1016/j.epsl.2008.06.038

Aitchison, J. C., & Davis, A. M. (2004). Evidence for the multiphase nature of the India-Asia collision from the Yarlung Tsangpo suture zone, Tibet. *Geological Society, London, Special Publications*, *226*(1), 217–233. https://doi.org/10.1144/gsl.sp.2004.226.01.12

Aitchison, J. C., Davis, A. M., Liu, J., Luo, H., Malpas, J. G., McDermid, I. R., et al. (2000). Remnants of a Cretaceous intra-oceanic subduction system within the Yarlung–Zangbo suture (southern Tibet). *Earth and Planetary Science Letters*, *183*(1–2), 231–244. https://doi.org/10.1016/s0012-821x(00)00287-9

Ali, J. R., & Aitchison, J. C. (2005). Greater India. *Earth-Science Reviews*, *72*(3–4), 169–188. https://doi.org/10.1016/j.earscirev.2005.07.005

An, W., Hu, X., Garzanti, E., Wang, J. G., & Liu, Q. (2021). New precise dating of the India-Asia collision in the Tibetan Himalaya at 61 Ma. *Geophysical Research Letters*, *48*(3), e2020GL090641. https://doi.org/10.1029/2020gl090641

Andrews-Speed, C., & Brookfield, M. (1982). Middle Paleozoic to Cenozoic geology and tectonic evolution of the northwestern Himalaya. *Tectonophysics*, *82*(3–4), 253–275. https://doi.org/10.1016/0040-1951(82)90048-8

Appel, E., Crouzet, C., & Schill, E. (2012). Pyrrhotite remagnetizations in the Himalaya: A review. *Geological Society, London, Special Publications*, *371*(1), 163–180. https://doi.org/10.1144/sp371.1

Beck, R. A., Burbank, D. W., Sercombe, W. J., Riley, G. W., Barndt, J. K., Berry, J. R., et al. (1995). Stratigraphic evidence for an early collision between northwest India and Asia. *Nature*, *373*(55), 55–58. https://doi.org/10.1038/373055a0

Besse, J., Courtillot, V., Pozzi, J., Westphal, M., & Zhou, Y. (1984). Palaeomagnetic estimates of crustal shortening in the Himalayan thrusts and Zangbo suture. *Nature*, *311*(5987), 621–626. https://doi.org/10.1038/311621a0

Bhutani, R., Pande, K., & Venkatesan, T. (2009). 40Ar–39Ar dating of volcanic rocks of the Shyok suture zone in north–west trans-Himalaya: Implications for the post-collision evolution of the Shyok suture zone. *Journal of Asian Earth Sciences*, *34*(2), 168–177. https://doi.org/10.1016/j.jseaes.2008.03.013

Bian, W., Yang, T., Ma, Y., Jin, J., Gao, F., Wang, S., et al. (2019). Paleomagnetic and geochronological results from the Zhela and Weimei Formations lava flows of the eastern Tethyan Himalaya: New insights into the breakup of eastern Gondwana. *Journal of Geophysical Research: Solid Earth*, *124*(1), 44–64. https://doi.org/10.1029/2018jb016403

Bian, W., Yang, T., Ma, Y., Jin, J., Gao, F., Zhang, S., et al. (2017). New Early Cretaceous palaeomagnetic and geochronological results from the far western Lhasa terrane: Contributions to the Lhasa-Qiangtang collision. *Scientific Reports*, *7*, 1–14. https://doi.org/10.1038/s41598-017-16482-3

Borneman, N. L., Hodges, K. V., Van Soest, M. C., Bohon, W., Wartho, J. A., Cronk, S. S., & Ahmad, T. (2015). Age and structure of the Shyok suture in the Ladakh region of northwestern India: Implications for slip on the Karakoram fault system. *Tectonics*, *34*(10), 2011–2033. https://doi.org/10.1002/2015tc003933

Bouilhol, P., Jagoutz, O. E., Hanchar, J. M., & Dudas, F. O. (2013). Dating the India–Eurasia collision through arc magmatic records. *Earth and Planetary Science Letters*, *366*, 163–175. https://doi.org/10.1016/j.epsl.2013.01.023

Brookfield, M., & Reynolds, P. (1981). Late Cretaceous emplacement of the Indus suture zone ophiolitic melanges and an Eocene-Oligocene magmatic arc on the northern edge of the Indian plate. *Earth and Planetary Science Letters*, *55*(1), 157–162. https://doi.org/10.1016/0012-821x(81)90094-7

Burg, J.-P., & Bouilhol, P. (2019). Timeline of the south Tibet–Himalayan belt: The geochronological record of subduction, collision, and underthrusting from zircon and monazite U–Pb ages. *Canadian Journal of Earth Sciences*, *56*(12), 1318–1332. https://doi.org/10.1139/cjes-2018-0174

Burg, J.-P., & Chen, G. (1984). Tectonics and structural zonation of southern Tibet, China. *Nature*, *311*(5983), 219–223. https://doi.org/10.1038/311219a0

Cao, Y., Sun, Z., Li, H., Pei, J., Jiang, W., Xu, W., et al. (2017). New Late Cretaceous paleomagnetic data from volcanic rocks and red beds from the Lhasa terrane and its implications for the paleolatitude of the southern margin of Asia prior to the collision with India. *Gondwana Research*, *41*, 337–351. https://doi.org/10.1016/j.gr.2015.11.006

Chapman, J. B., Robinson, A. C., Carrapa, B., Villarreal, D., Worthington, J., DeCelles, P. G., et al. (2018a). Cretaceous shortening and exhumation history of the South Pamir terrane. *Lithosphere*, *10*(4), 494–511. https://doi.org/10.1130/l691.1

Chapman, J. B., Scoggin, S. H., Kapp, P., Carrapa, B., Ducea, M. N., Worthington, J., et al. (2018b). Mesozoic to Cenozoic magmatic history of the Pamir. *Earth and Planetary Science Letters*, *482*, 181–192. https://doi.org/10.1016/j.epsl.2017.10.041

Chen, J., Huang, B., & Sun, L. (2010). New constraints to the onset of the India–Asia collision: Paleomagnetic reconnaissance on the Linzizong group in the Lhasa block, China. *Tectonophysics*, *489*(1–4), 189–209. https://doi.org/10.1016/j.tecto.2010.04.024

Chen, J., Huang, B., Yi, Z., Yang, L., & Chen, L. (2014). Paleomagnetic and $^{40}Ar/^{39}Ar$ geochronological results from the Linzizong group, Linzhou basin, Lhasa terrane, Tibet: Implications to Paleogene paleolatitude and onset of the India–Asia collision. *Journal of Asian Earth Sciences*, *96*, 162–177. https://doi.org/10.1016/j.jseaes.2014.09.007

Chen, W., Yang, T., Zhang, S., Yang, Z., Li, H., Wu, H., et al. (2012). Paleomagnetic results from the early cretaceous Zenong group volcanic rocks, Cuoqin, Tibet, and their paleogeographic implications. *Gondwana Research*, *22*(2), 461–469. https://doi.org/10.1016/j.gr.2011.07.019

Cloos, M. (1993). Lithospheric buoyancy and collisional orogenesis: Subduction of oceanic plateaus, continental margins, island arcs, spreading ridges, and seamounts. *Geological Society of America Bulletin*, *105*(6), 715–737. https://doi.org/10.1130/0016-7606(1993)105<0715:lbacos>2.3.co;2

Coutts, D. S., Matthews, W. A., & Hubbard, S. M. (2019). Assessment of widely used methods to derive depositional ages from detrital zircon populations. *Geoscience Frontiers*, *10*(4), 1421–1435. https://doi.org/10.1016/j.gsf.2018.11.002

Coward, M. P., Rex, D. C., Khan, M. A., Windley, B. F., Broughton, R. D., Luff, I. W., et al. (1986). Collision tectonics in the NW Himalayas. *Geological Society, London, Special Publications*, *19*(1), 203–219. https://doi.org/10.1144/gsl.sp.1986.019.01.11

Cowgill, E., Yin, A., Harrison, T. M., & Xiao-Feng, W. (2003). Reconstruction of the Altyn Tagh fault based on U-Pb geochronology: Role of back thrusts, mantle sutures, and heterogeneous crustal strength in forming the Tibetan Plateau. *Journal of Geophysical Research*, *108*(B7), 2346. https://doi.org/10.1029/2002jb002080

Crouzet, C., Gautam, P., Schill, E., & Appel, E. (2003). Multicomponent magnetization in western Dolpo (Tethyan Himalaya, Nepal): Tectonic implications. *Tectonophysics*, *377*(1–2), 179–196. https://doi.org/10.1016/j.tecto.2003.08.019

Dannemann, S., Appel, E., Rösler, W., Neumann, U., Liebke, U., & Nag, D. (2022). Palaeomagnetic indication for India–Asia collision at 12°N and maximum 810 km Greater India extent in the western suture zone. *Geophysical Journal International*, *229*(2), 1193–1211. https://doi.org/10.1093/gji/ggab528

DeCelles, P. G., Kapp, P., Ding, L., & Gehrels, G. E. (2007). Late Cretaceous to middle Tertiary basin evolution in the central Tibetan Plateau: Changing environments in response to tectonic partitioning, aridification, and regional elevation gain. *Geological Society of America Bulletin*, *119*(5–6), 654–680. https://doi.org/10.1130/b26074.1

DeCelles, P. G., Kapp, P., Gehrels, G., & Ding, L. (2014). Paleocene-Eocene foreland basin evolution in the Himalaya of southern Tibet and Nepal: Implications for the age of initial India-Asia collision. *Tectonics*, *33*(5), 824–849. https://doi.org/10.1002/2014tc003522

DeCelles, P. G., Robinson, D. M., & Zandt, G. (2002). Implications of shortening in the Himalayan fold-thrust belt for uplift of the Tibetan Plateau. *Tectonics*, *21*(6), 12-11–12-25. https://doi.org/10.1029/2001tc001322

Deenen, M. H., Langereis, C. G., van Hinsbergen, D. J., & Biggin, A. J. (2011). Geomagnetic secular variation and the statistics of palaeomagnetic directions. *Geophysical Journal International*, *186*(2), 509–520. https://doi.org/10.1111/j.1365-246x.2011.05050.x

Deenen, M. H., Langereis, C. G., van Hinsbergen, D. J., & Biggin, A. J. (2014). Erratum: Geomagnetic secular variation and the statistics of palaeomagnetic directions. *Geophysical Journal International*, *197*(1), 643. https://doi.org/10.1093/gji/ggu021

Dickinson, W. R., & Gehrels, G. E. (2009). Use of U–Pb ages of detrital zircons to infer maximum depositional ages of strata: A test against a Colorado Plateau Mesozoic database. *Earth and Planetary Science Letters*, *288*(1–2), 115–125. https://doi.org/10.1016/j.epsl.2009.09.013

Dunlap, W. J., & Wysoczanski, R. (2002). Thermal evidence for early Cretaceous metamorphism in the Shyok suture zone and age of the Khardung volcanic rocks, Ladakh, India. *Journal of Asian Earth Sciences*, *20*(5), 481–490. https://doi.org/10.1016/s1367-9120(01)00042-6

Dunlop, D. J., & Özdemir, Ö. (1997). *Rock magnetism: Fundamentals and frontiers. No. 3*. Cambridge University Press.

Dupont-Nivet, G., Lippert, P. C., van Hinsbergen, D. J., Meijers, M. J., & Kapp, P. (2010). Palaeolatitude and age of the Indo–Asia collision: Palaeomagnetic constraints. *Geophysical Journal International*, *182*(3), 1189–1198. https://doi.org/10.1111/j.1365-246x.2010.04697.x

Fisher, R. A. (1953). Dispersion on a sphere. *Proceedings of the Royal Society of London. Series A. Mathematical and Physical Sciences*, *217*(1130), 295–305. https://doi.org/10.1098/rspa.1953.0064

Gaetani, M., Garzanti, E., Jadoul, F., Nicora, A., Tintori, A., Pasini, M., & Khan, K. S. A. (1990). The North Karakorum side of the central Asia Geopuzzle. *Geological Society of America Bulletin*, *102*(1), 54–62. https://doi.org/10.1130/0016-7606(1990)102<0054:Tnksot>2.3.Co;2

Gaetani, M., Jadoul, F., Erba, E., & Garzanti, E. (1993). Jurassic and cretaceous orogenic events in the north Karakoram - Age constraints from sedimentary-rocks. *Geological Society, London, Special Publications*, *74*(1), 39–52. https://doi.org/10.1144/Gsl.Sp.1993.074.01.04

Gansser, A. (1964). Geology of the Himalayas.

Garming, J. F. L., Von Dobeneck, T., Franke, C., & Bleil, U. (2007). Low-temperature partial magnetic self-reversal in marine sediments by magnetostatic interaction of titanomagnetite and titanohematite intergrowths. *Geophysical Journal International*, *170*(3), 1067–1075. https://doi.org/10.1111/j.1365-246x.2007.03504.x

Garzanti, E., Baud, A., & Mascle, G. (1987). Sedimentary record of the northward flight of India and its collision with Eurasia (Ladakh Himalaya, India). *Geodinamica Acta*, *1*(4–5), 297–312. https://doi.org/10.1080/09853111.1987.11105147

Gehrels, G., Kapp, P. G., DeCelles, P., Pullen, A., Blakey, R., Weislogel, A., et al. (2011). Detrital zircon geochronology of pre-Tertiary strata in the Tibetan-Himalayan orogen. *Tectonics*, *30*(5), TC5016. https://doi.org/10.1029/2011tc002868

Gradstein, F. M., Ogg, J. G., Schmitz, M. D., & Ogg, G. M. (2020). *Geologic time scale 2020*. Elsevier.

He, J., Kapp, P., Chapman, J. B., DeCelles, P. G., & Carrapa, B. (2019). Structural setting and detrital zircon U–Pb geochronology of Triassic–Cenozoic strata in the eastern Central Pamir, Tajikistan. *Geological Society, London, Special Publications*, *483*(1), 605–630. https://doi.org/10.1144/sp483.11

Hu, B., Zhai, M., Li, T., Li, Z., Peng, P., Guo, J., & Kusky, T. M. (2012). Mesoproterozoic magmatic events in the eastern North China Craton and their tectonic implications: Geochronological evidence from detrital zircons in the Shandong Peninsula and North Korea. *Gondwana Research*, *22*(3–4), 828–842. https://doi.org/10.1016/j.gr.2012.03.005

Hu, X. M., Garzanti, E., An, W., & Hu, X. F. (2015). Provenance and drainage system of the Early Cretaceous volcanic detritus in the Himalaya as constrained by detrital zircon geochronology. *Journal of Palaeogeography*, *4*(1), 85–98. https://doi.org/10.3724/sp.j.1261.2015.00069

Huang, W. T., Dupont-Nivet, G., Lippert, P. C., van Hinsbergen, D. J., & Hallot, E. (2013). Inclination shallowing in Eocene Linzizong sedimentary rocks from southern Tibet: Correction, possible causes and implications for reconstructing the India–Asia collision. *Geophysical Journal International*, *194*(3), 1390–1411. https://doi.org/10.1093/gji/ggt188

Huang, W. T., Lippert, P. C., Jackson, M. J., Dekkers, M. J., Zhang, Y., Li, J., et al. (2017). Remagnetization of the Paleogene Tibetan Himalayan carbonate rocks in the Gamba area: Implications for reconstructing the lower plate in the India-Asia collision. *Journal of Geophysical Research: Solid Earth*, *122*(2), 808–825. https://doi.org/10.1002/2016jb013662

Huang, W. T., van Hinsbergen, D. J. J., Dekkers, M. J., Garzanti, E., Dupont-Nivet, G., Lippert, P. C., et al. (2015). Paleolatitudes of the Tibetan Himalaya from primary and secondary magnetizations of Jurassic to Lower Cretaceous sedimentary rocks. *Geochemistry, Geophysics, Geosystems*, *16*(1), 77–100. https://doi.org/10.1002/2014gc005624

Jagoutz, O. E., Bouilhol, P., Schaltegger, U., & Müntener, O. (2019). The isotopic evolution of the Kohistan Ladakh arc from subduction initiation to continent arc collision. *Geological Society, London, Special Publications*, *483*(1), 165–182. https://doi.org/10.1144/sp483.7

Jagoutz, O. E., Burg, J. P., Hussain, S., Dawood, H., Pettke, T., Iizuka, T., & Maruyama, S. (2009). Construction of the granitoid crust of an island arc part I: Geochronological and geochemical constraints from the plutonic Kohistan (NW Pakistan). *Contributions to Mineralogy and Petrology*, *158*(6), 739–755. https://doi.org/10.1007/s00410-009-0408-3

Jagoutz, O. E., Royden, L., Holt, A. F., & Becker, T. W. (2015). Anomalously fast convergence of India and Eurasia caused by double subduction. *Nature Geoscience*, *8*(6), 475–478. https://doi.org/10.1038/ngeo2418

Kaneko, Y., Katayama, I., Yamamoto, H., Misawa, K., Ishikawa, M., Rehman, H., et al. (2003). Timing of Himalayan ultrahigh-pressure metamorphism: Sinking rate and subduction angle of the Indian continental crust beneath Asia. *Journal of Metamorphic Geology*, *21*(6), 589–599. https://doi.org/10.1046/j.1525-1314.2003.00466.x

Kapp, P., & DeCelles, P. G. (2019). Mesozoic–Cenozoic geological evolution of the Himalayan-Tibetan orogen and working tectonic hypotheses. *American Journal of Science*, *319*(3), 159–254. https://doi.org/10.2475/03.2019.01

Kirschvink, J. L. (1980). The least-squares line and plane and the analysis of palaeomagnetic data. *Geophysical Journal International*, *62*(3), 699–718. https://doi.org/10.1111/j.1365-246x.1980.tb02601.x

Kirschvink, J. L., Kopp, R. E., Raub, T. D., Baumgartner, C. T., & Holt, J. W. (2008). Rapid, precise, and high-sensitivity acquisition of paleomagnetic and rock-magnetic data: Development of a low-noise automatic sample changing system for superconducting rock magnetometers. *Geochemistry, Geophysics, Geosystems*, *9*(5), Q05Y01. https://doi.org/10.1029/2007gc001856

Klootwijk, C., Sharma, M. L., Gergan, J., Shah, S., & Tirkey, B. (1984). The Indus-Tsangpo suture zone in Ladakh, Northwest Himalaya: Further palaeomagnetic data and implications. *Tectonophysics*, *106*(3–4), 215–238. https://doi.org/10.1016/0040-1951(84)90178-1

Klootwijk, C., Sharma, M. L., Gergan, J., Tirkey, B., Shah, S., & Agarwal, V. (1979). The extent of Greater India, II. Palaeomagnetic data from the Ladakh intrusives at Kargil, northwestern Himalayas. *Earth and Planetary Science Letters*, *44*(1), 47–64. https://doi.org/10.1016/0012-821x(79)90007-4

Lakhan, N., Singh, A. K., Singh, B. P., Sen, K., Singh, M. R., Khogenkumar, S., et al. (2020). Zircon U–Pb geochronology, mineral and whole-rock geochemistry of the Khardung volcanics, Ladakh Himalaya, India: Implications for Late Cretaceous to Palaeogene continental arc magmatism. *Geological Journal*, *55*(5), 3297–3320. https://doi.org/10.1002/gj.3594

Leloup, P. H., Arnaud, N., Lacassin, R., Kienast, J. R., Harrison, T. M., Trong, T. T. P., et al. (2001). New constraints on the structure, thermochronology, and timing of the Ailao Shan-Red River shear zone, SE Asia. *Journal of Geophysical Research*, *106*(B4), 6683–6732. https://doi.org/10.1029/2000jb900322

Li, Z., Ding, L., Song, P., Fu, J., & Yue, Y. (2017). Paleomagnetic constraints on the paleolatitude of the Lhasa block during the early cretaceous: Implications for the onset of India–Asia collision and latitudinal shortening estimates across Tibet and stable Asia. *Gondwana Research*, *41*, 352–372. https://doi.org/10.1016/j.gr.2015.05.013

Licht, A., Win, Z., Westerweel, J., Cogné, N., Morley, C. K., Chantraprasert, S., et al. (2020). Magmatic history of central Myanmar and implications for the evolution of the Burma Terrane. *Gondwana Research*, *87*, 303–319. https://doi.org/10.1016/j.gr.2020.06.016

Liebke, U., Appel, E., Ding, L., Neumann, U., Antolin, B., & Xu, Q. (2010). Position of the Lhasa terrane prior to India–Asia collision derived from palaeomagnetic inclinations of 53 Ma old dykes of the Linzhou basin: Constraints on the age of collision and post-collisional shortening within the Tibetan Plateau. *Geophysical Journal International*, *182*(3), 1199–1215. https://doi.org/10.1111/j.1365-246x.2010.04698.x

Liebke, U., Appel, E., Ding, L., & Zhang, Q. (2013). Age constraints on the India–Asia collision derived from secondary remanences of Tethyan Himalayan sediments from the Tingri area. *Journal of Asian Earth Sciences*, *62*, 329–340. https://doi.org/10.1016/j.jseaes.2012.10.012

Lippert, P. C., van Hinsbergen, D. J., & Dupont-Nivet, G. (2014). Early cretaceous to present latitude of the central proto-Tibetan Plateau: A paleomagnetic synthesis with implications for Cenozoic tectonics, paleogeography, and climate of Asia. *Geological Society of America Special Paper*, *507*, 1–21. https://doi.org/10.1130/2014.2507(01)

Ma, Y., Yang, T., Bian, W., Jin, J., Wang, Q., Zhang, S., et al. (2017). Paleomagnetic and geochronologic results of latest Cretaceous lava flows from the Lhasa terrane and their tectonic implications. *Journal of Geophysical Research: Solid Earth*, *122*(11), 8786–8809. https://doi.org/10.1002/2017jb014743

Ma, Y., Yang, T., Bian, W., Jin, J., Zhang, S., Wu, H., & Li, H. (2016). Early cretaceous paleomagnetic and geochronologic results from the Tethyan Himalaya: Insights into the Neotethyan paleogeography and the India–Asia collision. *Sci Rep-Uk*, *6*, 1–11. https://doi.org/10.1038/srep21605

Ma, Y., Yang, T., Yang, Z., Zhang, S., Wu, H., Li, H., et al. (2014). Paleomagnetism and U-Pb zircon geochronology of Lower Cretaceous lava flows from the western Lhasa terrane: New constraints on the India-Asia collision process and intracontinental deformation within Asia. *Journal of Geophysical Research: Solid Earth*, *119*(10), 7404–7424. https://doi.org/10.1002/2014jb011362

Martin, C. R., Jagoutz, O. E., Upadhyay, R., Royden, L. H., Eddy, M. P., Bailey, E., et al. (2020). Paleocene latitude of the Kohistan–Ladakh arc indicates multistage India–Eurasia collision. *Proceedings of the National Academy of Sciences of the United States of America*, *117*(47), 29487–29494. https://doi.org/10.1073/pnas.2009039117

Martin, C. R., Jagoutz, O. E., Upadhyay, R., van Tongeren, J. A., Mueller, P. A., & Weiss, B. P. (2023). Paleomagnetic constraints on the age of the Shyok suture zone [Dataset]. Dryad. https://doi.org/10.5061/dryad.ffbg79d0w

Meert, J. G., Pivarunas, A. F., Evans, D. A., Pisarevsky, S. A., Pesonen, L. J., Li, Z.-X., et al. (2020). The magnificent seven: A proposal for modest revision of the quality index. *Tectonophysics*, *790*, 228549. https://doi.org/10.1016/j.tecto.2020.228549

Meng, J., Wang, C., Zhao, X., Coe, R., Li, Y., & Finn, D. (2012). India-Asia collision was at 24 N and 50 Ma: Palaeomagnetic proof from southernmost Asia. *Scientific Reports*, *2*, 1–11. https://doi.org/10.1038/srep00925

Molnar, P., & Stock, J. M. (2009). Slowing of India's convergence with Eurasia since 20 Ma and its implications for Tibetan mantle dynamics. *Tectonics*, *28*(3), TC3001. https://doi.org/10.1029/2008tc002271

Mueller, P. A., Kamenov, G. D., Heatherington, A. L., & Richards, J. (2008). Crustal evolution in the southern Appalachian orogen: Evidence from Hf isotopes in detrital zircons. *The Journal of Geology*, *116*(4), 414–422. https://doi.org/10.1086/589311

Najman, Y., Jenks, D., Godin, L., Boudagher-Fadel, M., Millar, I., Garzanti, E., et al. (2017). The Tethyan Himalayan detrital record shows that India–Asia terminal collision occurred by 54 Ma in the Western Himalaya. *Earth and Planetary Science Letters*, *459*, 301–310. https://doi.org/10.1016/j.epsl.2016.11.036

Paton, C., Hellstrom, J., Paul, B., Woodhead, J., & Hergt, J. (2011). Iolite: Freeware for the visualisation and processing of mass spectrometric data. *Journal of Analytical Atomic Spectrometry*, *26*(12), 2508–2518. https://doi.org/10.1039/c1ja10172b

Patzelt, A., Li, H., Wang, J., & Appel, E. (1996). Palaeomagnetism of cretaceous to Tertiary sediments from southern Tibet: Evidence for the extent of the northern margin of India prior to the collision with Eurasia. *Tectonophysics*, *259*(4), 259–284. https://doi.org/10.1016/0040-1951(95)00181-6

Petterson, M. G., & Windley, B. F. (1985). RbSr dating of the Kohistan arc-batholith in the Trans-Himalaya of north Pakistan, and tectonic implications. *Earth and Planetary Science Letters*, *74*(1), 45–57. https://doi.org/10.1016/0012-821x(85)90165-7

Pullaiah, G., Irving, E., Buchan, K., & Dunlop, D. (1975). Magnetization changes caused by burial and uplift. *Earth and Planetary Science Letters*, *28*(2), 133–143. https://doi.org/10.1016/0012-821x(75)90221-6

Pundir, S., Adlakha, V., Kumar, S., & Singhal, S. (2020). Closure of India–Asia collision margin along the Shyok suture zone in the eastern Karakoram: New geochemical and zircon U–Pb geochronological observations. *Geological Magazine*, *157*(9), 1451–1472. https://doi.org/10.1017/s0016756819001547

Rai, H. (1982). Geological evidence against the Shyok palaeo-suture, Ladakh Himalaya. *Nature*, *297*(5862), 142–144. https://doi.org/10.1038/297142a0

Rex, A. J., Searle, M. P., Tirrul, R., Crawford, M. B., Prior, D. J., Rex, D. C., & Barnicoat, A. (1988). The geochemical and tectonic evolution of the central Karakoram, north Pakistan. *Philosophical Transactions of the Royal Society of London. Series A, Mathematical and Physical Sciences*, *326*, 229–255. https://doi.org/10.1098/rsta.1988.0086

Robinson, A. C., Ducea, M., & Lapen, T. J. (2012). Detrital zircon and isotopic constraints on the crustal architecture and tectonic evolution of the northeastern Pamir. *Tectonics*, *31*(2), TC2016. https://doi.org/10.1029/2011tc003013

Rolland, Y., Pecher, A., & Picard, C. (2000). Middle cretaceous back-arc formation and arc evolution along the Asian margin: The Shyok suture zone in northern Ladakh (NW Himalaya). *Tectonophysics*, *325*(1–2), 145–173. https://doi.org/10.1016/s0040-1951(00)00135-9

Rolland, Y., Picard, C., Pecher, A., Lapierre, H., Bosch, D., & Keller, F. (2002). The cretaceous Ladakh arc of NW Himalaya—Slab melting and melt–mantle interaction during fast northward drift of Indian Plate. *Chemical Geology*, *182*(2–4), 139–178. https://doi.org/10.1016/s0009-2541(01)00286-8

Rowley, D. B. (2019). Comparing paleomagnetic study means with apparent wander paths: A case study and paleomagnetic test of the greater India versus greater Indian basin hypotheses. *Tectonics*, *38*(2), 722–740. https://doi.org/10.1029/2017tc004802

Saktura, W. M., Buckman, S., Aitchison, J. C., & Zhou, R. (2021). Paleogene magmatic flex and flux in the Ladakh arc, NW Himalaya: Chronostratigraphy of the Khardung Formation. *Lithos*, *388*, 106053. https://doi.org/10.1016/j.lithos.2021.106053

Saktura, W. M., Buckman, S., Nutman, A. P., & Bennett, V. C. (2021). Late Jurassic Changmar complex from the Shyok ophiolite, NW Himalaya: A prelude to the Ladakh arc. *Geological Magazine*, *158*(2), 239–260. https://doi.org/10.1017/s0016756820000400

Schill, E., Appel, E., & Gautam, P. (2002). Towards pyrrhotite/magnetite geothermometry in low-grade metamorphic carbonates of the Tethyan Himalayas (Shiar Khola, Central Nepal). *Journal of Asian Earth Sciences*, *20*(3), 195–201. https://doi.org/10.1016/s1367-9120(01)00022-0

Searle, M. P. (2019). Timing of subduction initiation, arc formation, ophiolite obduction and India–Asia collision in the Himalaya. *Geological Society, London, Special Publications*, *483*(1), 19–37. https://doi.org/10.1144/sp483.8

Searle, M. P., Rex, A., Tirrul, R., Rex, D., Barnicoat, A., & Windley, B. (1989). Metamorphic, magmatic, and tectonic evolution of the central Karakoram in the Biafo-Baltoro-Hushe regions of northern Pakistan.

Sharma, K. K. (1987). Crustal growth and two-stage India-Eurasia collision in Ladakh. *Tectonophysics*, *134*(1–3), 17–28. https://doi.org/10.1016/0040-1951(87)90246-0

Sprain, C. J., Feinberg, J. M., Renne, P. R., & Jackson, M. (2016). Importance of titanohematite in detrital remanent magnetizations of strata spanning the Cretaceous-Paleogene boundary, Hell creek region, Montana. *Geochemistry, Geophysics, Geosystems*, *17*(3), 660–678. https://doi.org/10.1002/2015gc006191

Srimal, N. (1986). India-Asia collision: Implications from the geology of the eastern Karakoram. *Geology*, *14*(6), 523–527. https://doi.org/10.1130/0091-7613(1986)14<523:iciftg>2.0.co;2

Sun, Z., Jiang, W., Li, H., Pei, J., & Zhu, Z. (2010). New paleomagnetic results of Paleocene volcanic rocks from the Lhasa block: Tectonic implications for the collision of India and Asia. *Tectonophysics*, *490*(3–4), 257–266. https://doi.org/10.1016/j.tecto.2010.05.011

Sun, Z., Pei, J., Li, H., Xu, W., Jiang, W., Zhu, Z., et al. (2012). Palaeomagnetism of late Cretaceous sediments from southern Tibet: Evidence for the consistent palaeolatitudes of the southern margin of Eurasia prior to the collision with India. *Gondwana Research*, *21*(1), 53–63. https://doi.org/10.1016/j.gr.2011.08.003

Sundell, K. E., Gehrels, G. E., & Pecha, M. E. (2021). Rapid U-Pb geochronology by laser ablation multi-collector ICP-MS. *Geostandards and Geoanalytical Research*, *45*(1), 37–57. https://doi.org/10.1111/ggr.12355

Tahirkheli, R. K. (1979). Geology of Kohistan and adjoining Eurasian and Indo-Pakistan continents, Pakistan. *Geological Bulletin - University of Peshawar*, *11*, 1–30.

Tan, X., Gilder, S., Kodama, K. P., Jiang, W., Han, Y., Zhang, H., et al. (2010). New paleomagnetic results from the Lhasa block: Revised estimation of latitudinal shortening across Tibet and implications for dating the India–Asia collision. *Earth and Planetary Science Letters*, *293*(3–4), 396–404. https://doi.org/10.1016/j.epsl.2010.03.013

Tapponnier, P., Mattauer, M., Proust, F., & Cassaigneau, C. (1981). Mesozoic ophiolites, sutures, and arge-scale tectonic movements in Afghanistan. *Earth and Planetary Science Letters*, *52*(2), 355–371. https://doi.org/10.1016/0012-821x(81)90189-8

Tauxe, L. (2010). *Essentials of paleomagnetism*. University of California Press.

Tauxe, L., & Kent, D. V. (2004). A simplified statistical model for the geomagnetic field and the detection of shallow bias in paleomagnetic inclinations: Was the ancient magnetic field dipolar?

Tauxe, L., Kylstra, N., & Constable, C. (1991). Bootstrap statistics for paleomagnetic data. *Journal of Geophysical Research*, *96*(B7), 11723–11740. https://doi.org/10.1029/91jb00572

Tauxe, L., Shaar, R., Jonestrask, L., Swanson-Hysell, N., Minnett, R., Koppers, A., et al. (2016). PmagPy: Software package for paleomagnetic data analysis and a bridge to the magnetics Information Consortium (MagIC) database. [Software]. Geochemistry, Geophysics, Geosystems, *17*(6), 2450–2463. https://doi.org/10.1002/2016GC006307

Thanh, N. X., Rajesh, V., Itaya, T., Windley, B., Kwon, S., & Park, C.-S. (2012). A Cretaceous forearc ophiolite in the Shyok suture zone, Ladakh, NW India: Implications for the tectonic evolution of the Northwest Himalaya. *Lithos*, *155*, 81–93. https://doi.org/10.1016/j.lithos.2012.08.016

Thornburg, T. M., & Kulm, L. D. (1987). Sedimentation in the Chile Trench: Depositional morphologies, lithofacies, and stratigraphy. *Geological Society of America Bulletin*, *98*(1), 33–52. https://doi.org/10.1130/0016-7606(1987)98<33:sitctd>2.0.co;2

Tong, Y., Yang, Z., Pei, J., Li, J., Jin, S., Hou, L., et al. (2022). *New Late Cretaceous paleomagnetic results from the Lhasa terrane and their implications for the suturing of India and Eurasia and the closure of the Neo-Tethys Ocean*. GSA Bulletin.

Tong, Y., Yang, Z., Zheng, L., Yang, T., Shi, L., Sun, Z., & Pei, J. (2008). Early Paleocene paleomagnetic results from southern Tibet, and tectonic implications. *International Geology Review*, *50*(6), 546–562. https://doi.org/10.2747/0020-6814.50.6.546

Torsvik, T. H., Van der Voo, R., Preeden, U., Mac Niocaill, C., Steinberger, B., Doubrovine, P. V., et al. (2012). Phanerozoic polar wander, palaeogeography and dynamics. *Earth-Science Reviews*, *114*(3–4), 325–368. https://doi.org/10.1016/j.earscirev.2012.06.007

Upadhyay, R. (2014). Palaeogeographic significance of'Yasin-type'rudist and orbitolinid fauna of the Shyok suture zone, Saltoro Hills, northern Ladakh, India. *Current Science*, 223–228. Retrieved from https://www.jstor.org/stable/24099802

Upadhyay, R., Sinha, A. K., Chandra, R., & Rai, H. (1999). Tectonic and magmatic evolution of the eastern Karakoram, India. *Geodinamica Acta*, *12*(6), 341–358. https://doi.org/10.1016/s0985-3111(99)00101-1

Vaes, B., Li, S., Langereis, C. G., & van Hinsbergen, D. J. (2021). Reliability of palaeomagnetic poles from sedimentary rocks. *Geophysical Journal International*, *225*(2), 1281–1303. https://doi.org/10.1093/gji/ggab016

Van der Voo, R. (1990). The reliability of paleomagnetic data.

van Hinsbergen, D. J., Kapp, P., Dupont-Nivet, G., Lippert, P. C., DeCelles, P. G., & Torsvik, T. H. (2011). Restoration of Cenozoic deformation in Asia and the size of Greater India. *Tectonics*, *30*(5), TC5003. https://doi.org/10.1029/2011tc002908

van Hinsbergen, D. J., Lippert, P. C., Dupont-Nivet, G., McQuarrie, N., Doubrovine, P. V., Spakman, W., & Torsvik, T. H. (2012). Greater India basin hypothesis and a two-stage Cenozoic collision between India and Asia. *Proceedings of the National Academy of Sciences of the United States of America*, *109*(20), 7659–7664. https://doi.org/10.1073/pnas.1117262109

van Hinsbergen, D. J., Lippert, P. C., Li, S., Huang, W., Advokaat, E. L., & Spakman, W. (2019). Reconstructing Greater India: Paleogeographic, kinematic, and geodynamic perspectives. *Tectonophysics*, *760*, 69–94. https://doi.org/10.1016/j.tecto.2018.04.006

Vermeesch, P. (2021). Maximum depositional age estimation revisited. *Geoscience Frontiers*, *12*(2), 843–850. https://doi.org/10.1016/j.gsf.2020.08.008

Wang, J. G., Hu, X. M., Garzanti, E., An, W., & Liu, X. C. (2017). The birth of the Xigaze forearc basin in southern Tibet. *Earth and Planetary Science Letters*, *465*, 38–47. https://doi.org/10.1016/j.epsl.2017.02.036

Watson, G. (1956). A test for randomness of directions. *Geophysical Supplements to the Monthly Notices of the Royal Astronomical Society*, *7*, 160–161. https://doi.org/10.1111/j.1365-246x.1956.tb05561.x

Westerweel, J., Roperch, P., Licht, A., Dupont-Nivet, G., Win, Z., Poblete, F., et al. (2019). Burma Terrane part of the Trans-Tethyan arc during collision with India according to palaeomagnetic data. *Nature Geoscience*, *12*(10), 863–868. https://doi.org/10.1038/s41561-019-0443-2

Wu, F. Y., Ji, W. Q., Liu, C. Z., & Chung, S. L. (2010). Detrital zircon U–Pb and Hf isotopic data from the Xigaze fore-arc basin: Constraints on Transhimalayan magmatic evolution in southern Tibet. *Chemical Geology*, *271*(1–2), 13–25. https://doi.org/10.1016/j.chemgeo.2009.12.007

Xu, Y., Tan, X., Li, S., Li, Y., Ran, B., Han, Y., et al. (2022). Paleomagnetism of the Greater Indian passive margin sediments from the Upper Cretaceous succession: Evidence for long-delayed remagnetizations and implication for the India-Asia collision. *Journal of Asian Earth Sciences*, *229*, 105165. https://doi.org/10.1016/j.jseaes.2022.105165

Xue, W., Hu, X., Garzanti, E., Ma, A., Lai, W., & Li, C. (2022). Discriminating Qiangtang, Lhasa, and Himalayan sediment sources in the Tibetan Plateau by detrital-zircon UPb age and Hf isotope facies. *Earth-Science Reviews*, *236*, 104271. https://doi.org/10.1016/j.earscirev.2022.104271

Yang, T., Ma, Y., Bian, W., Jin, J., Zhang, S., Wu, H., et al. (2015a). Paleomagnetic results from the early cretaceous Lakang formation lavas: Constraints on the paleolatitude of the Tethyan Himalaya and the India–Asia collision. *Earth and Planetary Science Letters*, *428*, 120–133. https://doi.org/10.1016/j.epsl.2015.07.040

Yang, T., Ma, Y., Zhang, S., Bian, W., Yang, Z., Wu, H., et al. (2015b). New insights into the India–Asia collision process from Cretaceous paleomagnetic and geochronologic results in the Lhasa terrane. *Gondwana Research*, *28*(2), 625–641. https://doi.org/10.1016/j.gr.2014.06.010

Yi, Z., Huang, B., Chen, J., Chen, L., & Wang, H. (2011). Paleomagnetism of early Paleogene marine sediments in southern Tibet, China: Implications to onset of the India–Asia collision and size of greater India. *Earth and Planetary Science Letters*, *309*, 153–165. https://doi.org/10.1016/j.epsl.2011.07.001

Yi, Z., Wang, T., Meert, J. G., Zhao, Q., & Liu, Y. (2021). An initial collision of India and Asia in the equatorial humid belt. *Geophysical Research Letters*, *48*(9), e2021GL093408. https://doi.org/10.1029/2021gl093408

Yin, A., Harrison, T. M., Murphy, M., Grove, M., Nie, S., Ryerson, F., et al. (1999). Tertiary deformation history of southeastern and southwestern Tibet during the Indo-Asian collision. *Geological Society of America Bulletin*, *111*(11), 1644–1664. https://doi.org/10.1130/0016-7606(1999)111<1644:tdhosa>2.3.co;2

Yuan, J., Deng, C., Yang, Z., Krijgsman, W., Qin, H., Shen, Z., et al. (2022). Triple-stage India-Asia collision involving arc-continent collision and subsequent two-stage continent-continent collision. *Global and Planetary Change*, *212*, 103821. https://doi.org/10.1016/j.gloplacha.2022.103821

Yuan, J., Yang, Z., Deng, C., Krijgsman, W., Hu, X., Li, S., et al. (2021). Rapid drift of the Tethyan Himalaya terrane before two-stage India-Asia collision. *National Science Review*, *8*, nwaa173. https://doi.org/10.1093/nsr/nwaa173

Zaman, H., Otofuji, Y.-I., Khan, S. R., & Ahmad, M. N. (2013). New paleomagnetic results from the northern margin of the Kohistan Island Arc. *Arabian Journal of Geosciences*, *6*(4), 1041–1054. https://doi.org/10.1007/s12517-011-0432-2

Zaman, H., & Torii, M. (1999). Palaeomagnetic study of cretaceous red beds from the eastern Hindukush ranges, northern Pakistan: Palaeoreconstruction of the Kohistan–Karakoram composite unit before the India–Asia collision. *Geophysical Journal International*, *136*(3), 719–738. https://doi.org/10.1046/j.1365-246x.1999.00757.x

Zanchi, A., Poli, S., Fumagalli, P., & Gaetani, M. (2000). Mantle exhumation along the Tirich Mir fault zone, NW Pakistan: Pre-mid-Cretaceous accretion of the Karakoram terrane to the Asian margin. *Geological Society, London, Special Publications*, *170*(1), 237–252. https://doi.org/10.1144/gsl.sp.2000.170.01.13

Zhang, Y., & Huang, B. (2017). The influence of Cretaceous paleolatitude variation of the Tethyan Himalaya on the India-Asia collision pattern. *Science China Earth Sciences*, *60*(6), 1057–1066. https://doi.org/10.1007/s11430-016-9042-7

Journal of Geophysical Research: Solid Earth

Supporting Information for

Paleomagnetic Constraint on the Age of the Shyok Suture Zone

Craig R. Martin[1,2], Oliver Jagoutz[1], Rajeev Upadhyay[3], Jill A. van Tongeren[4], Paul A. Mueller[5], and Benjamin P. Weiss[1]

[1] *Department of Earth, Atmospheric, and Planetary Sciences, Massachusetts Institute of Technology, Cambridge, MA 02139, U.S.A.*

[2] *Department of Earth and Planetary Sciences, University of Texas at Austin, Austin, TX 78712, USA.*

[3] *Department of Geology, Kumaun University, Nainital, Uttarakhand, 263001, India.*

[4] *Department of Earth and Climate Sciences, Tufts University, Medford MA 02155, U.S.A*

[5] *Department of Geological Sciences, University of Florida, Gainesville, FL 32611, U.S.A.*

Contents of this file

Figures S1 to S10

Additional Supporting Information (Files uploaded separately)

Tables S1 to S6

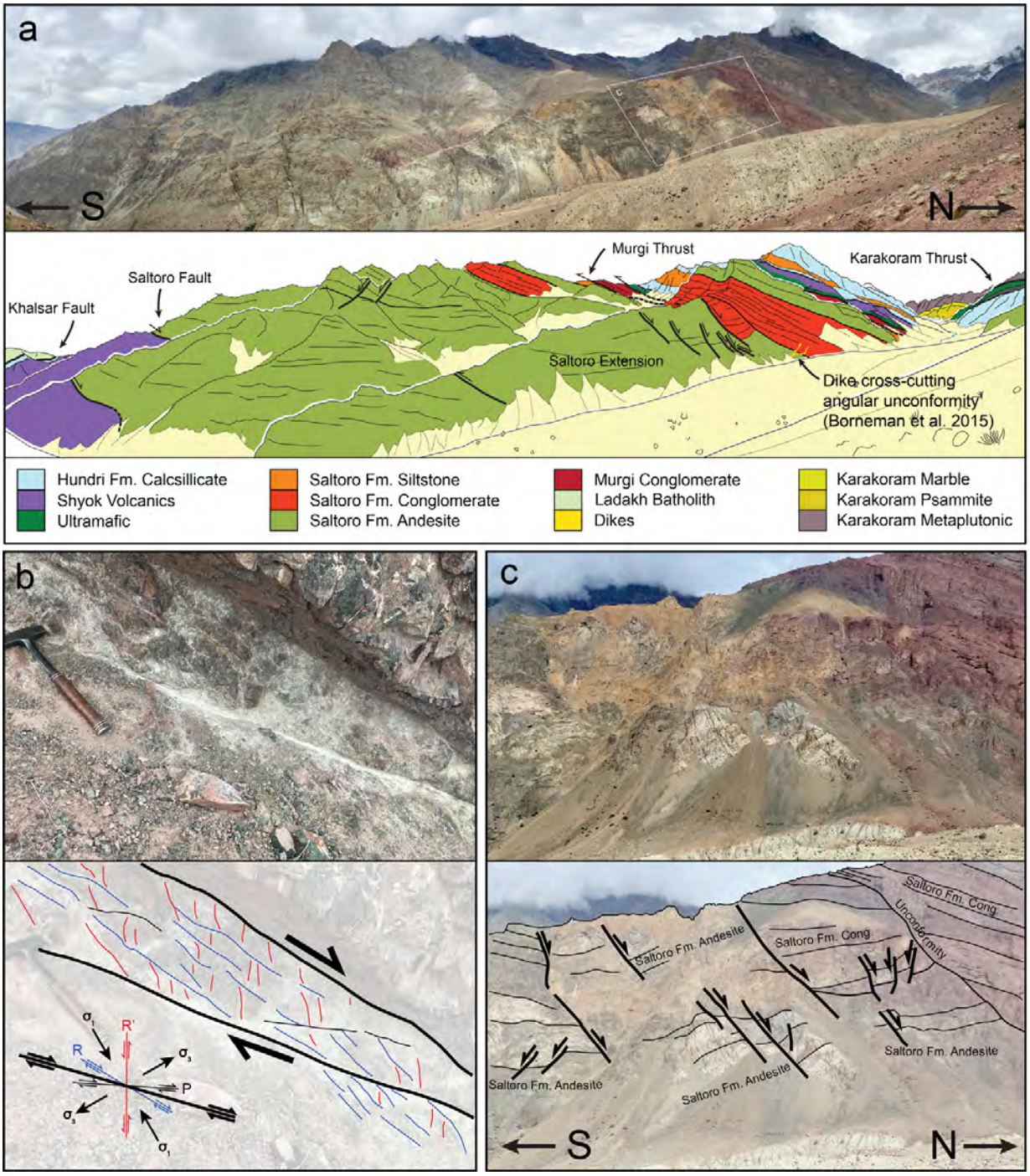

Figure S1: a) Panorama sketch of the Udmaru Valley showing the lower Saltoro Formation volcanics in faulted contact with the underlying Shyok Volcanics. The figure also shows the extensional faults in the Saltoro Formation, and the buttress unconformity at the base of the upper Saltoro Formation, which is crosscut by the Shukur dikes. The Murgi thrust and overlying deformed repetition of the Shyok suture zone can be seen truncating the top of the Saltoro Formation to the right of the sketch. **b)** Reidel shear planes in the fault surface of a fault near the base of the Saltoro Formation in the Udmaru area. The orientation of R-type reidel shear planes

are shown in blue, R'-type planes are shown in red and P-type planes are shown in black. **c)** Expanded view of the faulted area in the lower Saltoro Formation. Saltoro Formation andesite layering and andesitic agglomerates are displaced by normal faults with 10 – 30 m displacements and are overlain by Saltoro Formation conglomerates, the normal faults do not extend above the angular unconformity.

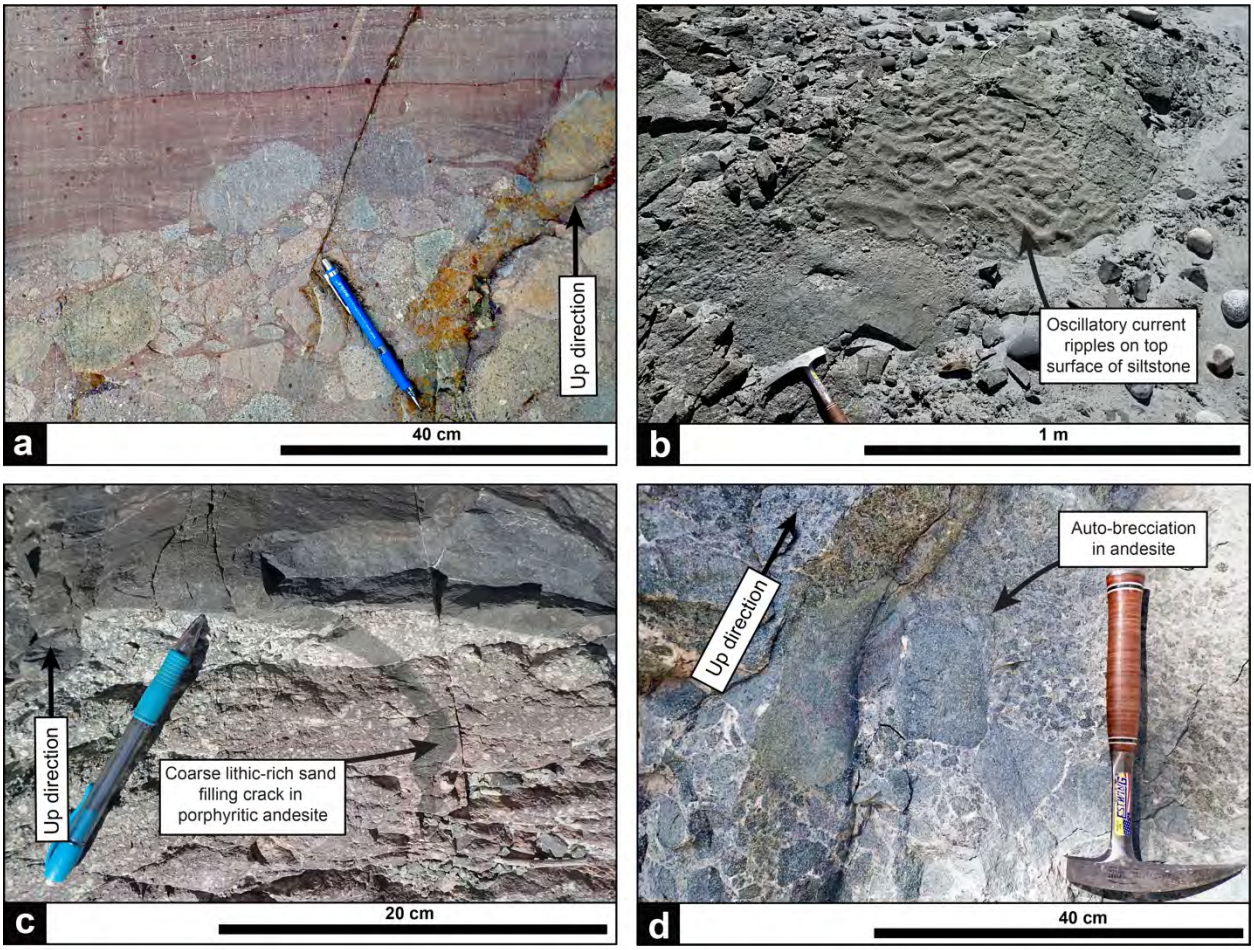

Figure S2: Images depicting a range of Saltoro formation rock types. a) Upper contact of clast-supported conglomerate overlain by laminated silty sandstone. Conglomerate clasts of mostly volcanic origin are poorly sorted and range in size from small pebbles to cobbles with variable shapes from sub-rounded to sub-angular. Sandy and silty laminations in the sandstone can be seen onlapping against the pebbles at the contact indicating the paleo-up direction. b) Small oscillatory current ripples ripples in upper surface of tilted siltstone bed exposed near Charasa Monastery indicating an estuarine or low-energy fluvial environment. c) A coarse, lithic-rich sandstone infills cracks in the underlying plagioclase-pyroxene porphyritic andesite. The surface of the outcrop has rugosities that appear to crosscut the infilled crack, but these are not penetrative d) An example of magmatic brecciation in a basaltic flow near the top of the Saltoro stratigraphy, suggesting that some of the flows were erupted into water or flowed into water rich environments.

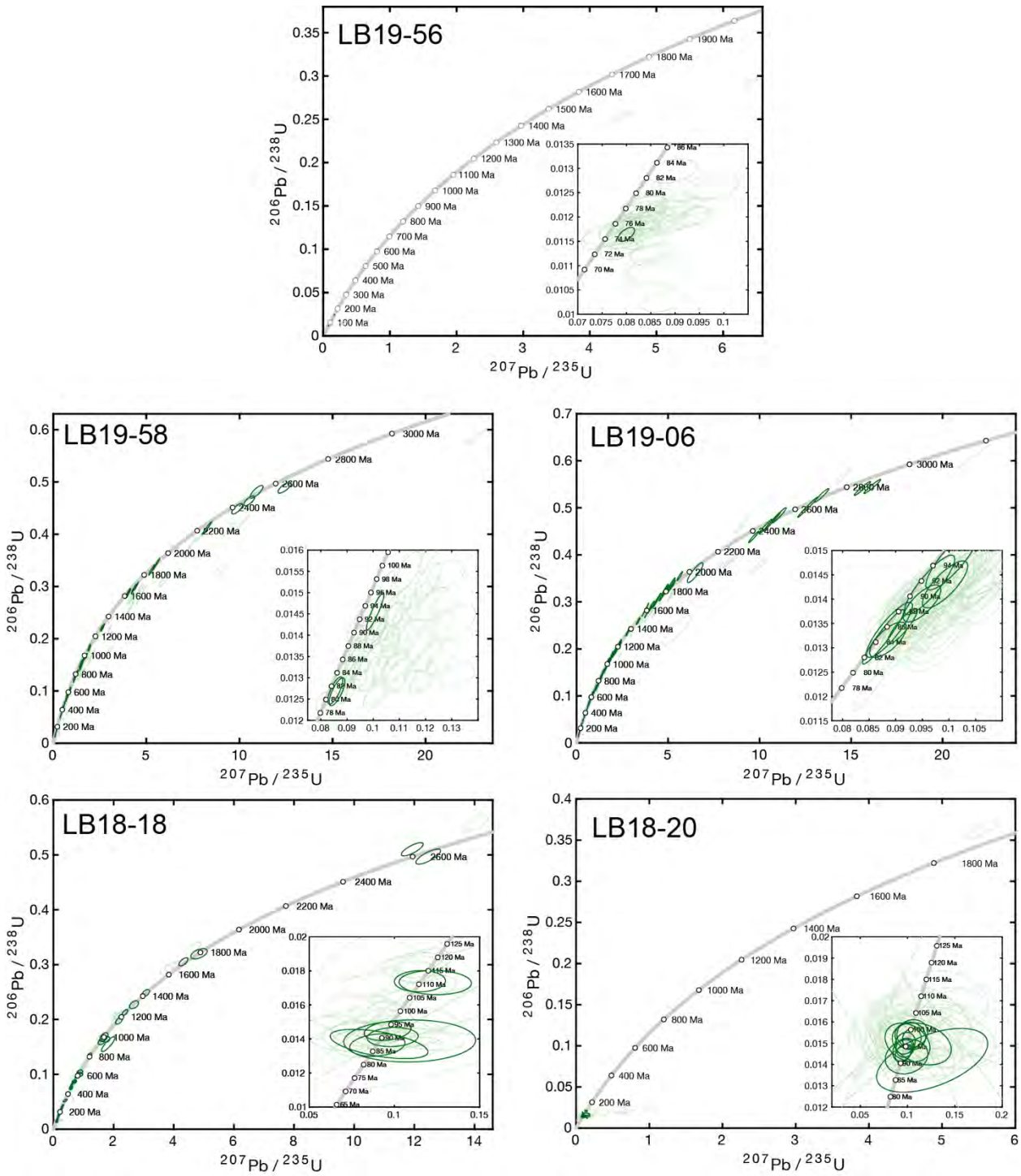

Figure S3: U-Pb isotopic data presented using Wetherill concordia diagrams with 2σ uncertainties. Smaller inlay Wetherill concordia diagrams show the youngest populations of grains in each sample. Dark green symbols indicate zircons that passed the filtration criteria (≤5% discordance and 206Pb/204Pb ≤ 0.001) while light green symbols indicate zircons that were excluded based on their failure to meet the same criterion.

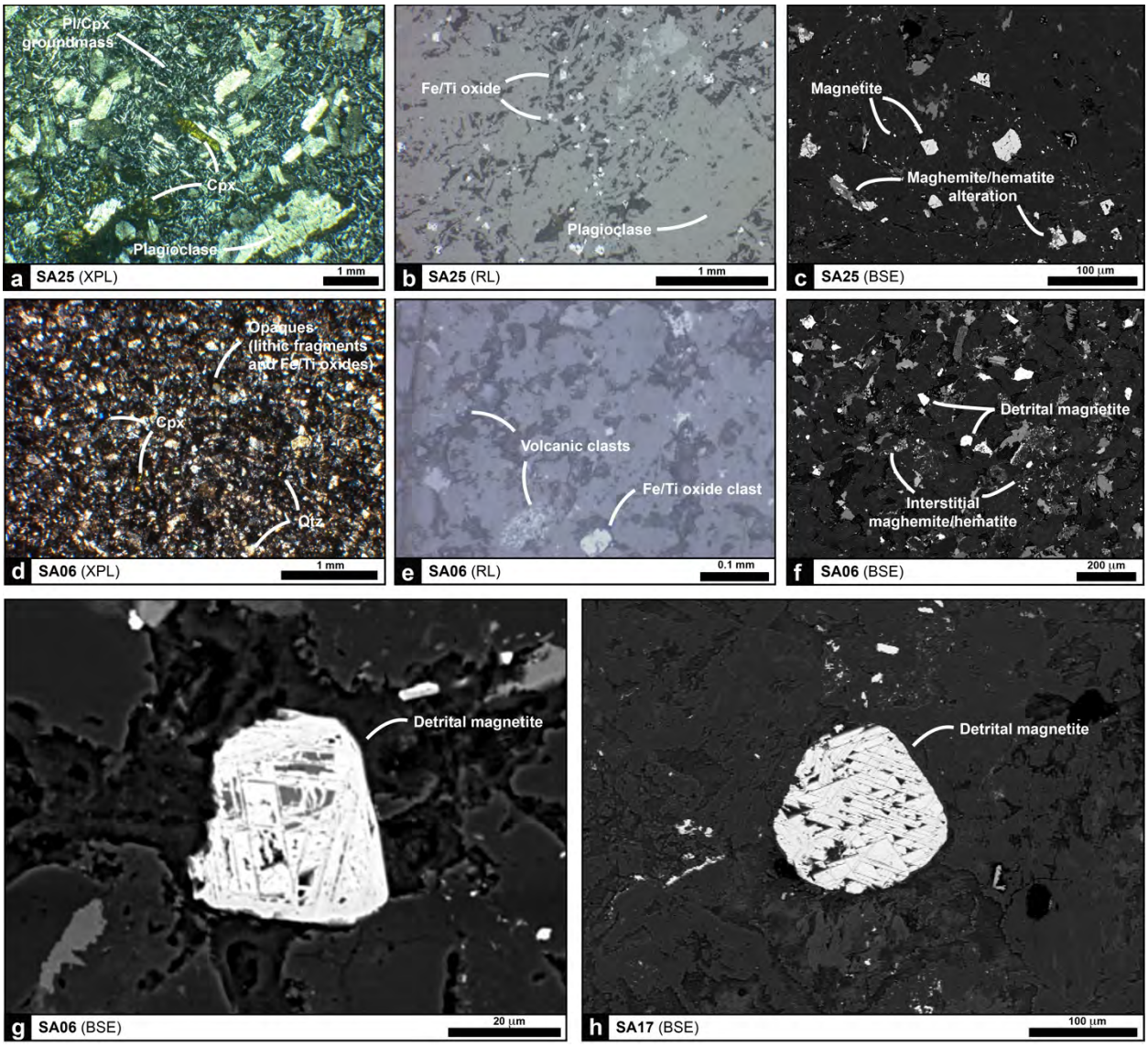

Figure S4: Photomicrographs and backscattered electron (BSE) images of Saltoro Formation samples. **a)** cross-polarized transmitted light (XPL) image of andesite flow from site SA25, **b)** reflected light (RL) image of andesite volcanic from site SA25, **c)** BSE image of sample SA25 showing primary magnetite/titanomagnetite and titanohematite/hematite alteration, **d)** cross-polarized transmitted light (XPL) image of siltstone from site SA06, **e)** reflected light (RL) image of siltstone from site SA06, **f)** BSE image of sample SA25 showing primary magnetite/titanomagnetite and titanohematite/hematite alteration, **g-h)** BSE images of magnetite grains in sites SA06 and SA17 exhibiting rounded corners indicative of detrital transport.

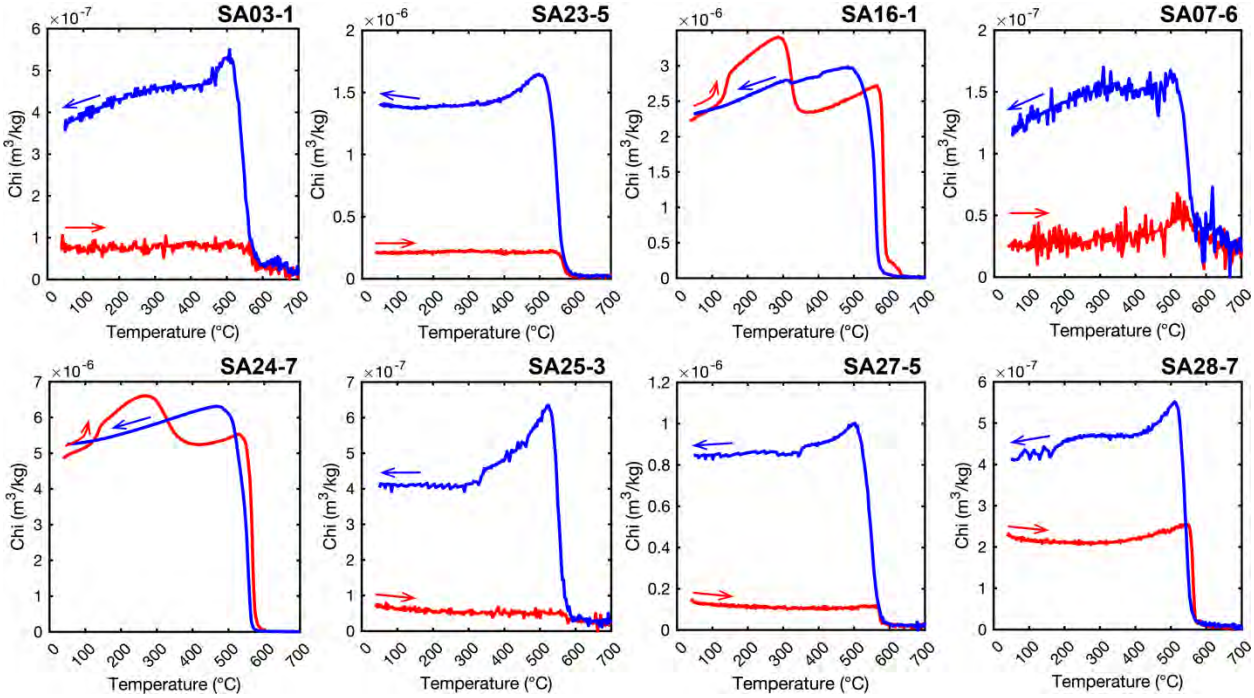

Figure S5: Normalized susceptibility versus temperature for a suite of representative samples. The top row shows samples from sedimentary sites, the bottom row shows samples from andesitic volcanic sites. Red curves represent the susceptibility changes with increasing temperature during heating, and blue curves represent susceptibility changes with decreasing temperature during cooling.

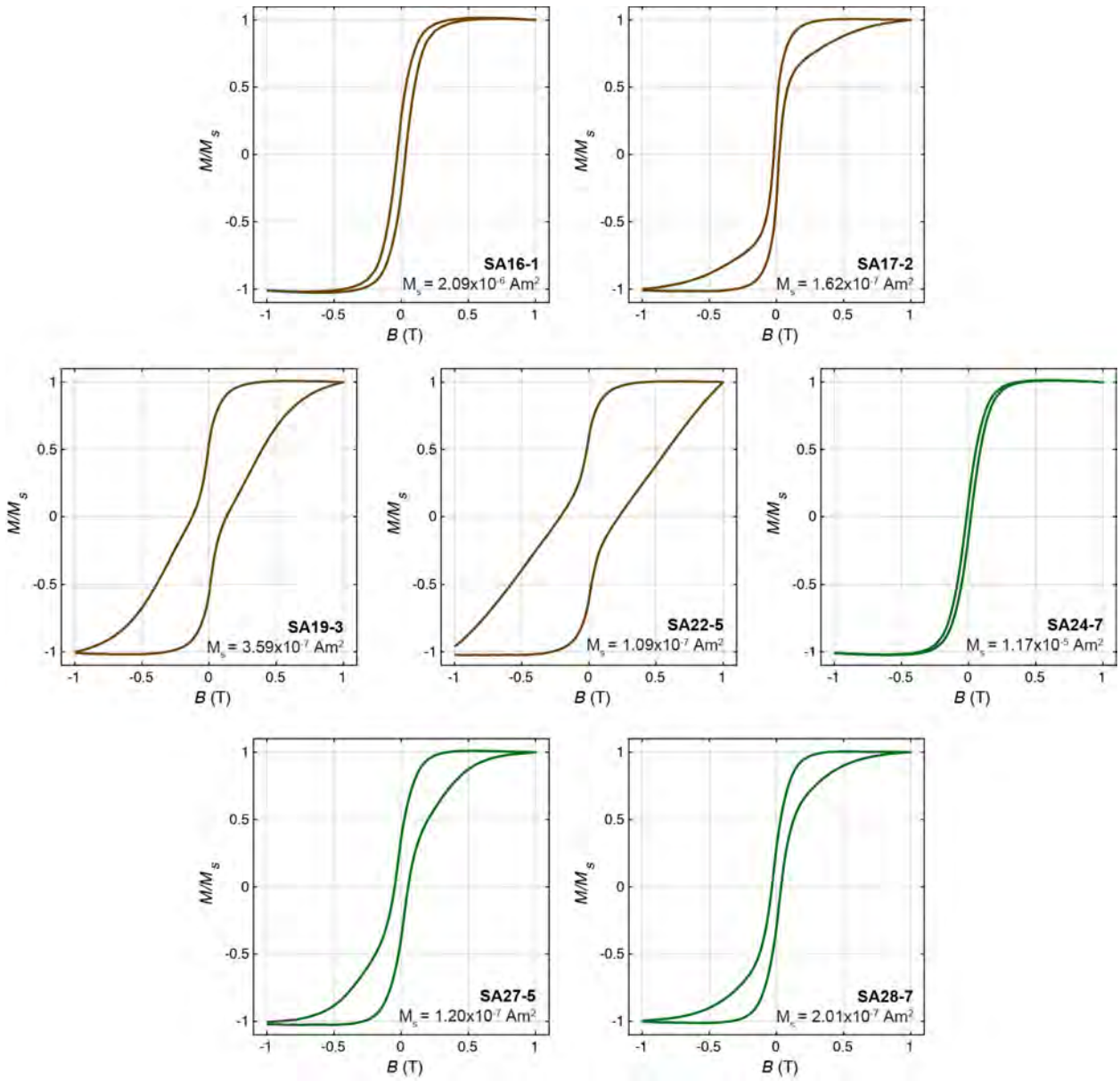

Figure S6: Hysteresis curves for four representative sediment samples (brown curves) and three representative volcanic samples (green curves). Hysteresis loops were acquired for applied fields of B = -1.0 – 1.0 T and were corrected by removing any paramagnetic or diamagnetic signals. The corrected curves were used to ascertain the saturation magnetization (M_s), the saturation remanent magnetization (M_{rs}), the coercivity of remanence (H_{cr}) and the coercivity (H_c) for each sample.

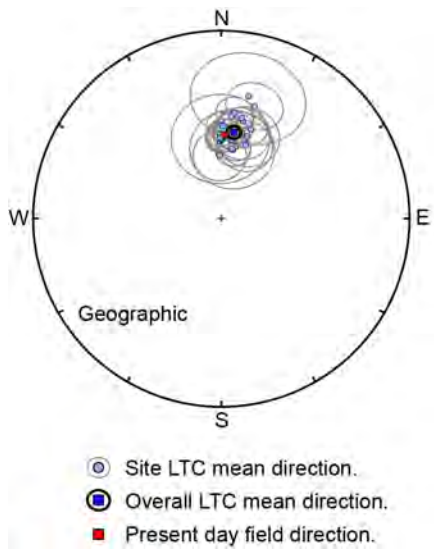

Figure S7: Equal area projection showing the LCT site-mean directions and their a95 uncertainty ellipses. The mean direction of the LCT components is almost equivalent to the modern-day field direction. Negative inclinations are projected onto the upper hemisphere and shown with open symbols, filled symbols represent positive inclinations.

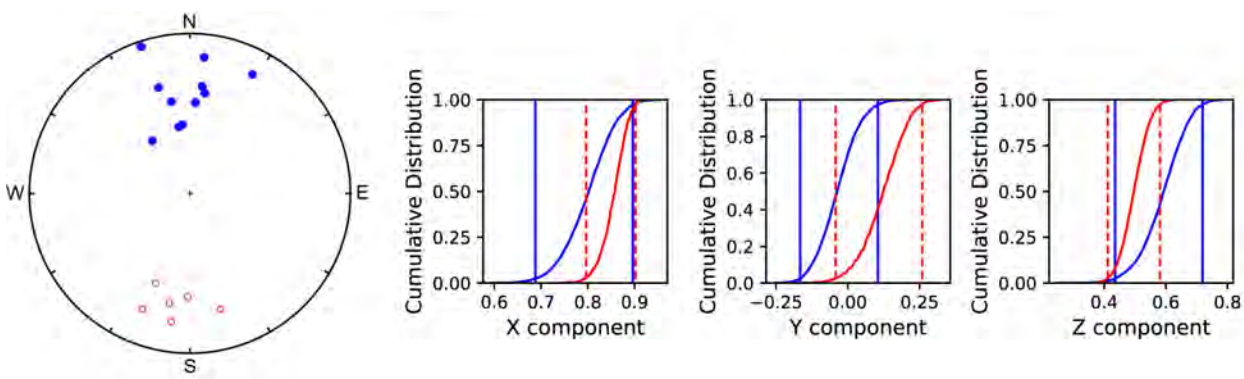

Figure S8: Cumulative distributions of Cartesian components of bootstrapped means from 1000 pseudo-samples from tilt-corrected, E/I corrected and VAR corrected site-mean direction data. The 95% confidence intervals for the two populations overlap in X, Y, and Z. The two populations can be considered antipodal to one another because they share a common mean, passing a reversal test.

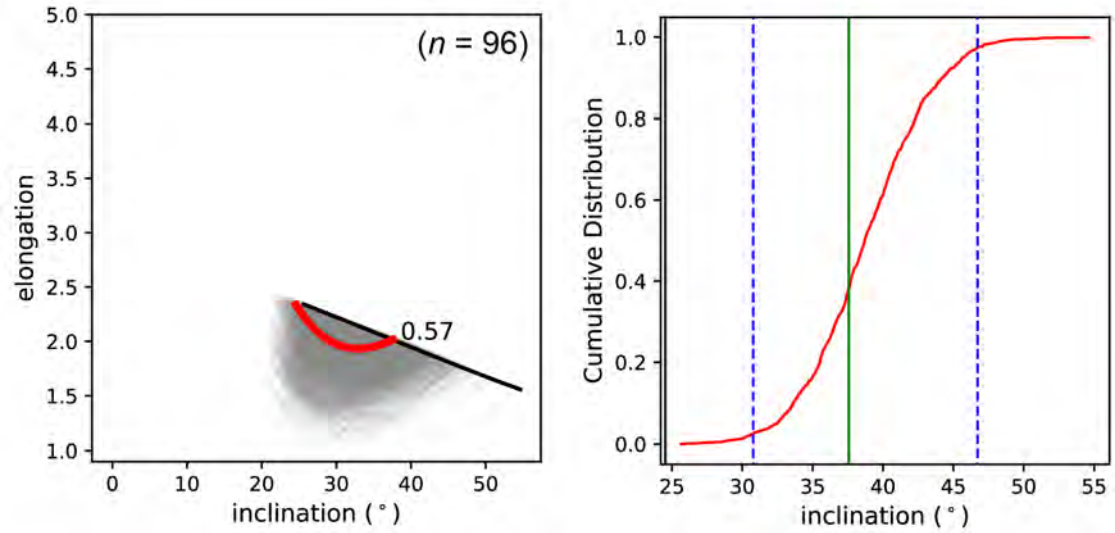

Figure S9: Results of Tauxe and Kent (2004) E/I method to determine flattening factor for *n* = 96 sedimentary sample directions. The upper left figure shows elongation versus inclination predicted by the TK03 geocentric axial dipole model (black curve), elongation versus inclination upon stepwise unflattening of the data set by decreasing the flattening factor (*f*) (red curve), and the results of stepwise unflattening of 1000 bootstrap pseudo-samples (grey curves). The intersection between the red and black curves is used to determine the flattening factor that is then used to correct the sedimentary site-mean directions for inclination shallowing. The right figure shows a cumulative distribution of the 1000 bootstrap runs (red curve) along with the uncorrected inclination (black line) and the corrected inclination (green line) as well as it's 95% uncertainty (blue dashed lines).

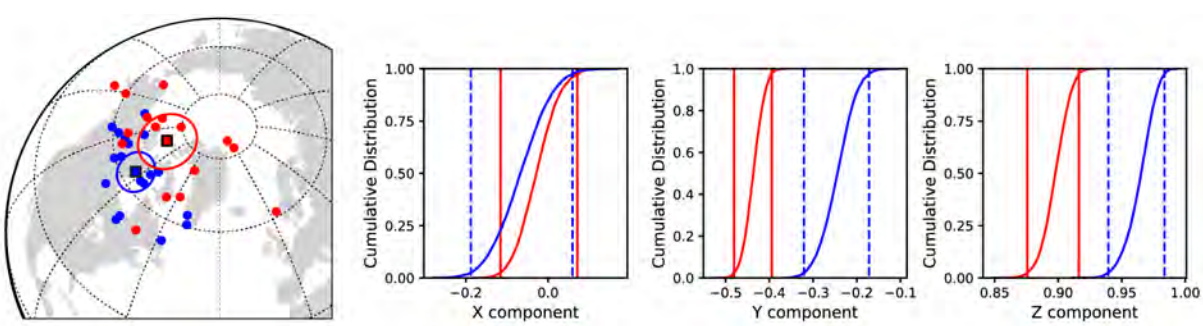

Figure S10: Cumulative distributions of Cartesian components of bootstrapped means from 1000 pseudo-samples from Saltoro formation VGP distribution (red) and Khardung formation VGP distribution (blue). The 95% confidence intervals for the two populations do not overlap in Y, and Z. Therefore, the two populations cannot be considered to share a common mean direction.